1 **Demonstration of the refined three-dimensional structure of**

2 **mesoscale eddies and computational error estimates via**

3 **Lagrangian Analysis**

4 YIN Heqing[1], DAI Haijin[1*], ZHANG Weimin[1,2], ZHANG Xueyan[1], WANG

5 Pinqiang[1]

6 **[1]College of Meteorology and Oceanography, National University of Defense Technology,**

7 **Changsha 410073, China**

8 **[2]Laboratory of Software Engineering for Complex Systems, Changsha 410073, China**

9

10 **Abstract**

11 In previous studies, Lagrangian analyses were used to assess large-scale ocean

12 circulation, and the Lagrangian coherent structure could also reveal the evolution of

13 the two-dimensional structure of the mesoscale eddies. However, few studies have

14 demonstrated the three-dimensional structure of the mesoscale eddies via Lagrangian

15 analysis. Compared with previous studies, which investigated the eddy structure via a

16 Eulerian view, we used a Lagrangian view to provide a different perspective to study

17 the eddy structure. An idealized cyclonic mesoscale eddy is built up over a seamount,

18 and it presents downwelling inside the eddy and upwelling alongside the eddy formed

19 within a closed circulation system. This structure is difficult to display via a Eulerian

20 analysis. However, the trajectories of particles can well demonstrate the full cycle: the

21 fluid sank and rotated inside the eddies, converged to the upwelling zone of the

22 bottom layer and returned to the surface through upwelling. We also applied a

23 Lagrangian analysis to a realistic simulation. As a significant phenomenon in the

24 South China Sea, the dipole structure of the anticyclonic eddy (AE)/cyclonic eddy

25 (CE) pair off of central Vietnam has been well studied but mainly at the sea surface.

26 With a Lagrangian analysis, we illustrate the three-dimensional structure of the eddy

27 pair: the fluid sank (rose) and rotated inside the AE (CE). More importantly, the

28 trajectories of the particles suggested that there was no fluid exchange between the

29 two eddies since the strong boundary jet separates them from each other. All the

30 conclusions above have been verified and are supported by the computational error

31 estimate. With a selected time step and integral period, the computational errors

32 always present small values, although they increase with strong divergent and vertical

33 diffusive flow.

34 **Key words:** mesoscale eddy, Lagrangian Analysis, three-dimensional structure.

1. Introduction

Oceans exhibit a huge range of dynamical motions, large scale motions (> 300 km), mesoscale motions (50-300 km), submesoscale motions (1-50 km) and small scale motions (<1 km) (McWilliams, 2016; Torres et al., 2018; Zhang et al., 2019). In slow-varying seawater, tracers (i.e., salt, heat, dissolved oxygen) carried by the fluid particles are used as seawater motion indicators. From a microscopic view, a particle is considered as a collection of a huge amount of molecules. Thus, velocity of the particle is defined as the mass weighted mean of the velocities of the individual molecules. When a great amount of fluid particles are integrated with three-dimensional (3D), time-evolving velocity fields, the trajectories of the particles depict the structure of the fluid field, which is the basis of the Lagrangian analysis.

Previous studies suggested that Lagrangian analysis was able to capture the primary structures of large-scale circulations both in the atmosphere (Kjellsson and Döös, 2012) and the ocean (Döös et al., 2008). However, the Hadley Cell (Deacon Cell) is a slow-varying and quasi-phase-locked phenomenon in the atmosphere (ocean) with a spatial scale of thousands of kilometers and kilometers in the horizontal and vertical directions, respectively. We sought to determine how the Lagrangian analysis performs for a smaller scale phenomenon with a varying velocity both in spatial and temporal dimensions. The typical phenomenon that comes to mind is the mesoscale eddy. As one of the most important mesoscale ocean phenomena, eddies have diameters of approximately 5-120 km and orbital velocities of 0.5-0.7 m/s (Johannessen et al., 1987; Adams et al., 2017). Strong mesoscale eddies can extend to several hundreds of meters in the vertical direction. Lin (Lin et al., 2018) traced a considerable number of tracers in a mesoscale eddy using a Lagrangian analysis, although they did not report the structure of the mesoscale eddy. In this study, the structure of the mesoscale eddy becomes our first priority to concern about.

To test how the Lagrangian analysis performs in demonstrating the 3D structure of the mesoscale eddy. We firstly build up an idealized eddy, which has a clearer and

31   simpler 3D structure, compared with the real eddies in the ocean. In the second step,

32   we try to apply the Lagrangian analysis to a realistic mesoscale eddy, which is from

33   the results of   numerical simulation. As a robust phenomenon in the South China

34   Sea(SCS), a dipole structure of anticyclonic eddy - cyclonic eddy (AE/CE) pair

35   appears off the central Vietnam (Wang et al. 2006; Chu et al., 2014). The eddy

36   generation mechanism is still debatable between three viewpoints. One suggests that

37   the eddy pair is generated by the boundary jet, which is induced by the summer

38   monsoon (Kuo et al., 2000; Xie et al., 2003; Wang et al., 2006). Wang et al. (2006)

39   suggested the jet contains strong baroclinic instability. The dipole structure of wind

40   stress curl (wind-driven) and the continental slope (potential vorticity conservation)

41   are considered as the other two eddy generation mechanisms (Fang et al., 2002),

42   although Fang et al. (2002) suggested the wind stress curl should be the dominant

43   reason... The AE/CE pair usually is generated in June, reached its maximum intensity

44   in August or September and disappeared in October. Eulerian analyses usually focus

45   on the current structure at the surface. However, the Lagrangian analysis can well

46   demonstrate the 3D structure of the eddy pair.

47

48   On the other hand, previous studies have usually neglected to provide computational

49   error estimates with their experimental settings (i.e., time step, integration period).

50   However, the computational error may be as large as hundreds of kilometers, which is

51   even larger than the diameter of the mesoscale eddy. In this study, assume

52   approximately constant mesoscale eddies in the idealized simulation, while employ

53   the time-varying current in the realistic simulation; we demonstrated the structure of

54   the mesoscale eddies using a Lagrangian analysis. We also provide estimates of the

55   computational error obtained using different experimental settings to improve the

56   reliability of our results.

57

58   This paper is arranged as follows. In Section 2, we introduce the Lagrangian

59   calculation tool. In Section 3, we analyzed the ideal eddy as an application of this

60   tool. In Section 4, we analyzed the AE/CE pair as an application of this tool. In

61   Section 5, we provide a summary and identify future research topics.

62   **2.   Introduction to the Lagrangian analysis method**

63   The Lagrangian calculation tool implemented here (Sebille et al., 2018) begins with

64   an analysis the output from general circulation models (i.e., general ocean circulation

65   model or general atmospheric circulation model) or other velocity data. The velocity

66   would be interpolated into the coordinate redefined for further analysis. Usually, the

67   interpolation methods in the horizontal directions (i.e., bilinear interpolation) are

68   different from that in the vertical direction (i.e., tension spline curve). The distance

69   that the particle undergoes is estimated with implicit, explicit or semi-implicit

70   iterative methods (i.e., 4th order Runge-Kutta scheme (RK4)) both in the spatial and

71   temporal dimensions. Together with the initial location and the movement vector, the

72   new transient location of the particle is estimated. The Lagrangian trajectory of the

73   particle is depicted with a considerable number of transient locations.

74

75   When the actual trajectory of a particle is divided into n parts, each part of its

76   trajectory can be viewed as the journey of the particle during a short period.

77   Considering that the particle has a velocity of (u_n,v_n,w_n) and undergoes a period of δt

78   from (u_n,v_n,w_n) to $(u_{n+1},v_{n+1},w_{n+1})$, there is

$$x_{n+1} = x_n + u_n\delta t \quad (1)$$
$$y_{n+1} = y_n + v_n\delta t \quad (2)$$
$$z_{n+1} = z_n + w_n\delta t \quad (3)$$

82   Realistically, the current varies in different locations and its trajectory during a given

83   period may be a curve. Furthermore, we considered that each particle has the same

84   velocity during one time step in the model; thus, a computational error (Fig. 1) was

85   introduced using the Lagrangian calculation. Fortunately, as long as we employ a

86   small time step and use the Lagrangian calculation within a reasonable period, we can

87   maintain the computational error within an acceptable range. When we demonstrate

88   the 3D structure of the eddy using Lagrangian calculations in the following sections,

89   we always maintained a sufficiently short time step and integral period to maintain

90   acceptable computational errors.

91

The Lagrangian calculation tool used in this study is the Lagrangian TRANSport
model (LTRANS), which is an off-line particle-tracking model that runs with the
stored predictions of a three-dimensional (3D) hydrodynamic model, i.e., Regional
Oceanic Modelling System (ROMS, Shchepetkin and McWilliams, 2005; Lemariè et
al., 2012). LTRANS can simulate passive particles or particles with sinking or
floating behaviors, i.e., sediment, oil droplets or planktonic organisms (we used the
passive particle option in this study). LTRANS is designed to track the trajectories of
particles in three dimensions.

In this study, ROMS was employed to simulate the idealized and realistic mesoscale
eddies. However, the method of producing these eddies is not a focus of this study. As
a result, additional details on the production of the idealized mesoscale eddy with
ROMS is introduced in Appendix A. The Eulerian analysis of the idealized mesoscale
eddy is also described in Appendix A. Similarly, more detail about how we reproduce
the AE/CE eddy pair off the central Vietnam with ROMS-4DVAR is introduced in
Appendix B. Eulerian analysis of the AE/CE eddy pair is also presented in Appendix
B.

3. Demonstrate the refined structure of cyclonic mesoscale eddies over a
   seamount via a Lagrangian analysis

In order to apply a Lagrangian analysis to the mesoscale eddy, we first employed an
idealized mesoscale eddy, whose structure is clearer and simpler than the realistic
oceanic mesoscale eddy. The idealized mesoscale eddy was produced by the
generation mechanism of baroclinic instability, we also employed a seamount to
ensure that this eddy did not move.

The primary mesoscale eddy was located in the middle of this domain, where the
seamount is set beneath. The current moved cyclonically (Fig. 2a, vector), which
indicates a positive vorticity (Fig. 2a, shading). To better depict the outline of the
mesoscale eddy, the eddy boundary is defined as follows (Okubo, 1970; Weissa,

122   1991):

123    $$W = s_{sh}^2 + s_{st}^2 - \zeta^2 \qquad (4)$$

124    $$EddyBoundary = -0.6 * std(W) \quad (5)$$

125   where s_{sh} and s_{st} are the shear and strain deformation, respectively, ζ is the vertical

126   component of vorticity, and std(W) is the standard deviation of W.

127

128   Based on the eddy boundary definition, the diameter of the primary eddy is

129   approximately 29 km at the surface (Fig. 2a, green line). The eddy boundary

130   definition is applied to the lower layers, and the outline of the mesoscale eddy is

131   depicted (Fig. 2b, green line). The eddy was nearly a cylinder above 180 m and then

132   shrank at greater depths, and its diameter was only 3 km at a depth of 210 m before it

133   widened to 13 km at a depth of 245 m. The distribution of the vorticity suggested that

134   the current moved cyclonically above 180 m and moved anticyclonically in lower

135   layers (Fig. 2c). The current moved faster at the surface and slower in deeper layers;

136   and the distribution of the current speed was similar in each layer (not given).

137

138   *3.1 Experiment settings for Lagrangian analysis of idealized mesoscale eddy*

139   Using the Lagrangian analysis, we first studied the two-dimensional (2D) structure.

140   By assuming that particles were always floating in the same layer, we neglected

141   vertical motion for the sake of simplicity. As the computational error increased with

142   faster flow, the surface and bottom layers were chosen for demonstration. Since the

143   velocity distribution was similar in the upper layers, we felt that the surface layer was

144   a good choice. In Exp1 and Exp2, the time steps were set to 60 s. We also chose 5

145   additional time steps ranging from 1 to 600 s to test the sensitivity of the

146   computational error. At the sea surface, we released the particles outside the

147   mesoscale eddy (Exp1 and Assum Exp1). At the bottom layer, we released the

148   particles near the seamount (Exp2 and Assum Exp2). Assum Exp* indicates the

149   sensitivity experiments of Exp*. More details are shown in Table 1.

150

151   In the 3D structure demonstration, we added vertical motion. To assess the sensitivity

152 of the computational error, we used 6 time steps ranging from 1 to 600 s as in the 2D

153 structure experiment. To demonstrate the 3D structure of the mesoscale eddy or

154 visualize the upwelling and downwelling, we released the particles at the surface eddy

155 boundary (Exp3 and Assum Exp3) and in the bottom layer (Exp4, Assum Exp4, Exp5

156 and Assum Exp5) and chose the particles that formed the mesoscale eddy for analysis.

157 More details are shown in Table 1.

158

159 As the experiment used in this study is idealized, we assumed that the trajectory

160 calculated with a time step of 1 s approximates the "real trajectory", which is much

161 smaller than the actual time step in the ROMS model (15 s) and was used to estimate

162 the computational error obtained with different time step selections.

163

164 Table 1. Experimental settings for the Lagrangian analysis applied to the idealized

165 mesoscale eddy.

name	displayed dimensions	time step (second)	location where particles released	integration period (hour)	released particle number
Exp1	2 (x-y)	60	surface eddy boundary	800	1000
Exp2	2 (x-y)	60	the bottom of the seamount	800	1000
Exp3	3 (x-y-z)	30	surface eddy boundary	800	5000
Exp4	3 (x-y-z)	30	upwelling zone at the bottom layer	800	10000
Exp5	3 (x-y-z)	30	the bottom of the seamount	800	10000
Assum Exp1	2 (x-y)	1, 5, 30, 300, 600	surface eddy boundary	800	100×5
Assum	2 (x-y)	1, 5, 30,	the bottom of the	800	100×5

Exp2		300, 600	seamount		
Assum Exp3	3 (x-y-z)	1, 5, 60, 300, 600	surface eddy boundary	800	100×5
Assum Exp4	3 (x-y-z)	1, 5, 60, 300, 600	upwelling zone in the bottom layer	800	100×5
Assum Exp5	3 (x-y-z)	1, 5, 60, 300, 600	the bottom of the seamount	800	100×5

3.2 Two-dimensional structure of the eddy

We released the particles at the boundary of the mesoscale eddy at the sea surface (Exp1), and the particles started to move close to the center of the eddy. Meanwhile, the particles rotated cyclonically (Fig. 3a). The particles arrived at the center of the eddy in 400 hours. We performed the same experiment in the lower layers of the eddy; as long as the vorticity was positive, the trajectories of the particles shared similar velocity distributions.

We released the particles at the bottom of the seamount (Fig. 3b, Exp2), and they moved against the seamount and remained where upwelling eventually occurred. In the south-north direction, the particles moved in the direction of upwelling. In the east-west direction, however, when the particles reached the upwelling zone, they moved towards the center of the upwelling and rotated cyclonically based on the vorticity distribution. The particles remained nearly static after 250 hours and 400 hours in the south-north and east-west directions, respectively.

3.3 Three-dimensional structure of the eddy

The calculation of 3D flow became more complex, and the computational error grew to reach unexpected values. To describe the eddy structure, we should explain two important features. First, we should describe how the particles moved in the mesoscale eddy. The Eulerian view (Appendix A) suggested that downwelling

188 occurred inside the primary mesoscale eddy. We released the particles at the sea

189 surface and outside the mesoscale eddy (Exp3). Over time, the particles sunk down to

190 lower layers due to downwelling (Fig. 4a), and the color distribution in the vertical

191 direction suggested that the vertical velocity in the mesoscale eddy was relatively

192 uniform. The particles also rotated cyclonically as they moved towards the center of

193 the eddy and reached the central part in 400 hours. When the particles reached the

194 seamount, which was located outside the eddy, the particles sunk along the slope,

195 reached the bottom layers, and moved upwards due to upwelling. We also released

196 particles close to the boundary of the mesoscale eddy in lower layers, and most of

197 these particles shared similar trajectories.

198

199 The particles released at the surface demonstrated the structure inside the mesoscale

200 eddy. Next, we demonstrated the source of these particles as a second feature of the

201 mesoscale eddy. We released the particles in the upwelling zone at the bottom layer

202 (Exp4, Fig. 4b), and their trajectories were different with those released at the bottom

203 of the seamount (Exp5, Fig. 4c). These trajectories suggested that the particles

204 released in the upwelling zone could flow to the surface layer. A vertical view

205 suggested that these particles moved upward to the surface via upwelling near the

206 north-south boundary and in the center of the upwelling zone on the eastern and

207 western sides of the seamount (Fig. 4d), where these particles eventually remained in

208 the 2D experiment (Fig. 3b). Another issue we found is that the particles entered the

209 eddy in different layers. The lower the layer in which the particles entered the eddy

210 was, the shorter the period they needed. We released the particles in different layers,

211 and some of them entered the mesoscale eddy while the rest remained outside the

212 mesoscale eddy. However, the results suggested that only the particles released in the

213 upwelling zone at the bottom layer could travel back to the surface layer.

214

215 The 3D structure of the mesoscale eddy was described as the rotation and then sinking

216 of the water inside the eddy down to its lower layers. The water flowed out from the

217 bottom of the eddy and along the slope of the seamount to reach the bottom layer.

218 Because of strong convergence, the water outside the eddy was sucked into the eddy

219 in its upper layers, and it was compensated by the water particles transported by

220 upwelling from lower layers or by downwelling from upper layers (not shown).

221 However, the source of the water in the surface layer could only be derived from the

222 bottom layer and transported via upwelling surrounding the mesoscale eddy.

223

224 ***3.4 Computational error estimate and discussion***

225 Sensitivity experiments, which are introduced in Table 1, were employed for

226 estimating and discussing the computational error.

227

228 *3.4.1   Time step and integration period*

229 In the 2D experiments (Exp1, Assum Exp1, Exp2 and Assum Exp2), the

230 computational errors generally increase with larger time steps. At the sea surface

231 (Exp1 and Assum Exp1, Fig. 5a), the magnitude of the computational error always

232 maintained at a small amplitude (no more than 0.045 km) in the convergent flow.

233 However, the computational errors grow gradually in the bottom layer (Exp2 and

234 Assum Exp2) since divergent flow occurs. The computational error grew as much as 6

235 km (Fig. 5b), which was 100 times greater than that at the sea surface. However, we

236 found that when the time step was smaller than 60 s, the maximum computational

237 error was no more than 1 km, which meant that the particles may have stayed in the

238 same grid and shared the same physical features. In conclusion, we suggest that the

239 time step in the Lagrangian analysis of 2D flow should be smaller than 60 s and that

240 the trajectory should be calculated over a long time period (e.g., 500 hours).

241

242 In the 3D experiments, the computational errors grew slowly in a convergent flow

243 (Exp3 and Assum Exp3, Fig. 3c). When the particles moved in the eddy with an

244 integration period of less than 450 hours, the computational error was always

245 maintained below 1 km. Outside the eddy (Exp4, Assum Exp4, Exp5 and Assum

246 Exp5), however, the computational error increased up to 40 km (Fig. 3d) after 450

247 hours of integration. When the time step was smaller than 60 s, the computational

248 error could be maintained at small values for a long period. In contrast, when the time

249 step was longer than 300 s, the computational error grew significantly and could not

250 be ignored in a short integration period.

251

252 We need to make a note here. **The discussion above focused on the worst**

253 **trajectory simulation.** However, for **most (85%) of the particles' trajectories, the**

254 **computational error could always be maintained below 2 km over 800 hours of**

255 **integration** when the time step is smaller than 60 s (not given). In summary, when the

256 time step of the Lagrangian analysis is no more than 60 s, the simulations of most of

257 the particles' trajectories are acceptable. If we only integrate the Lagrangian analysis

258 for 450 hours, nearly all the trajectories are acceptable.

259

260 *3.4.2 Current features*

261 The computational error is determined not only by the model setting (i.e., the time

262 step and integration period) but also by the current features. In this study, we checked

263 several current features, such as divergence, vorticity, vertical velocity shear and

264 current speed. In general, the correlation coefficient between the current feature and

265 the growth rate of the computation error increases (Fig. 6), as the time step gets larger

266 (larger computational error). The growth rate of the computational error is equivalent

267 to growth of the computational error during a short period, i.e., 1 hour. In the

268 upwelling, the correlation coefficient between the divergence (Fig. 6a; vertical

269 velocity shear, Fig. 6b; current speed, Fig. 6c) and the growth rate of the

270 computational error is more than 0.2 (0.17, 0.07), which indicates that a faster current

271 or flow with larger vertical shear and divergence may increase the computational

272 error. On the other hand, the correlation coefficient between the vertical vorticity and

273 the growth rate of the computational error (Fig. 6d) is nearly -0.08, which means that

274 strong anticyclonic rotation may increase the computational error. In the

275 downwelling, the correlation coefficient between the divergence (Fig. 6e; vertical

276 velocity shear, Fig. 6f) and the growth rate of computational error is nearly 0.18

277 (0.27), which is consistent with the results in the upwelling. However, the correlation

278　coefficient between the current speed and the growth rate of computational error (Fig.

279　6g) is -0.02, which is inconsistent with the result for the upwelling, and the relation is

280　not significant. The correlation coefficient between the vertical vorticity and the

281　growth rate of computational error (Fig. 6h) is only -0.14, which is much smaller than

282　that in the upwelling. As a result, we conclude that the growth rate of computational

283　error is determined by the divergence and vertical velocity shear, and it may also be

284　influenced by the vertical vorticity. However, the current speed may not determine the

285　growth rate of the computational error. (Note: Because the number of the samples is

286　as large as 80,000, when the correlation coefficient is larger than 0.06, it should

287　achieve significance based on the t-test.)

288

289　**4.　Demonstrate the dipole structure of cyclonic and anticyclonic eddies near**

290　　　**Vietnam with Lagrangian analysis**

291　West part of SCS (106°E~116°E, 4°N~18°N) was simulated with the regional ocean

292　model ROMS, which has a horizontal resolution of 1/20°. An additional strong

293　constraint 4D-Var (I4DVAR) scheme (Moore et al., 2011) is also implemented to

294　perform the data assimilation with the satellite observations (sea surface temperature

295　(SST), sea level anomaly (SLA)) and in situ T/S profile (Argo, Conductivity-

296　Temperature-Depth recorder (CTD) and etc.). More details are presented in Appendix

297　B.

298

299　The AE/CE pair located in the region of [8-14N, 109-113E] (Fig. 9 a, b) is consistent

300　with the observations through the whole September. Take the current distribution on

301　September 13, 2013 as a typical example. The eddy boundary defined here is not OW,

302　and we followed the definition by Dong (Dong et al., 2012) and Nencioli (Nencioli et

303　al., 2010). The AE mainly occurred in the upper 350 m. Across the AE/CE pair (Fig.

304　7a, green line), there is eastward flow in the south (north) part of the CE (AE), while

305　westward flow (Fig. 7c) appears in the north (south) part of the CE (AE), which

306　indicated that the current rotated cyclonically (anticyclonically) in the CE (AE). As a

307　result, downwelling (upwelling) appeared in the AE (CE), although the vertical

308 motion is not totally horizontally uniform inside the eddies. Disturbed by the vertical

309 flow, the isotherms (Fig. 7d, blue contour) sank (lifted) in the AE (CE). Although the

310 AE is stronger than the CE and has a larger radius (Fig. 7a), the CE (Fig. 7b blue line)

311 extended to deeper layers than the AE (more details are shown in Appendix B).

312

313 *4.1 Lagrangian analysis experiment settings*

314 Following Section 3.1, we first studied the 2D structure of the AE/CE pair. The

315 scenario can be viewed as we tracked the floating tracers (i.e., Argo, glider) in the

316 same layer. Thus, we neglected vertical motion and released the particles at the upper

317 layer (z=-28 m, where the vertical motion began to become significant in CE, |w|>

318 0.124 mm/s) between the eddy center and eddy boundary both in the AE and CE

319 (Exp6, current is considered as constant as that on September 13, 2013). In Exp6, the

320 time step was set to 60 s. We also selected another 5 time steps ranging from 1 to 600

321 s to test the sensitivity of the computational error. The sensitivity experiments were

322 named as Assum Exp6, which were corresponding to Exp6. More details are shown in

323 Table 2.

324

325 In the 3D structure demonstration, we added vertical motion. To assess the sensitivity

326 of the computational error, we used 6 time steps ranging from 1 to 600 s as in the 2D

327 structure experiment. The particles are released in the whole layers both in the CE

328 (Assum Exp7) and in the AE (Assum Exp8). However, to better reveal the realistic

329 water motion inside the dipole eddy-pair, we applied the Lagrangian analysis to time-

330 varying current field, which is from the realistic simulation results, to demonstrate the

331 3D structure of the mesoscale eddy. We released the particles at the same location as

332 Exp6 (only in the AE, Exp7). We also released the particles at the lower layer of AE

333 (z=-352 m, where it is the bottom of CE, Exp8) and selected the particles that formed

334 the mesoscale eddy for analysis. In the Exp7 and Exp8, we released the particles on

335 September 1, and the Lagragian analysis is integrated through the whole September,

336 with the corresponding simulation.

337

338 Table 2. Experiment settings for the Lagrangian analysis applied to the eddy pair

339 simulation (Vietnam dipole).

name	displayed dimensions	time step (second)	location where particles released	integration period (hour)	released particle number
Exp6	2 (x-y)	60	z=-28 m, AE, CE, in the middle between the eddy center and the eddy boundary	1440	5600×2
Exp7	3 (x-y-z)	30	same as Exp6, but only in AE.	720	6000
Exp8	3 (x-y-z)	30	z=-352 m, CE, in the middle between the eddy center and the eddy boundary	720	6000
Assum Exp6	2 (x-y)	1, 5, 30, 300, 600	same as Exp6	1440	600×5
Assum Exp7	3 (x-y-z)	1, 5, 30, 60, 300, 600	through the layer z=-28 to z=-352, in the middle between the eddy center and the eddy boundary, but only in CE	1440	300×6
Assum Exp8	3 (x-y-z)	1, 5, 30, 60, 300, 600	same as Assum Exp7, but in AE	1440	300×6

340

4.2 2D structure of the AE/CE pair

342 In the upper layer (z=-28 m, Exp6, Fig. 8a, b), we release the particles inside the AE

343 and CE. Convergence occurs in the AE, and the particles move closer to the center of

344 the AE after 1440-hour integration (Fig. 8a), whereas divergence occurs in the CE,

345 and the particles spread toward outside the CE, and reached as far as 200 km after

346 1440-hour integration (Fig. 8b). Meanwhile, the particles rotated anticyclonically.

347

4.3 3D structure of the AE/CE pair

Based on the distribution of the flow, the particles motion was relatively simple in the AE/CE eddy pair. Particles were released in the upper layer of AE (Exp7, Fig. 9a, b) and sank to lower layers gradually since there was mostly downwelling inside the AE. However, the particles were eventually located in different depths at the end of the experiment, which indicated that vertical motion is not horizontally uniform inside the AE. A typical particle can well demonstrate how the flow moved inside the AE, and we found that the particle sank from -28 m to -262 m (Fig. 9b) and rotated anticyclonically.

Similarly, particles were released in the lower layer of CE (Exp8, Fig. 9c, d) and gradually moved upward to upper layers (Fig. 9c). The wavy distribution in the vertical direction suggested that the upwelling is not horizontally uniform inside the CE. We also employed one particle to demonstrate the structure of the flow inside the CE (Fig.9d). We found that the particle rose from -352 m to shallower than -52 m after 720 hours of integration, and it rotated anticyclonically. The results suggested that vertical motion is stronger in the AE than the CE, which is consistent with our earlier conclusion. On the other hand, we found that fluid exchange did not occur between the AE and CE. The boundary jet likely separates these two eddies and made them independent from each other.

4.4 Computational error and sensitivity test

Sensitivity experiments, which are introduced in Table 2, were employed to estimate and discuss the computational error.

4.4.1 Time step and integration period

In the 2D experiment, the computational error is always maintained at a very small value in the convergent flow (Fig. 10a), even when we use a time step as large as 600 s. In the divergent flow, however, the maximum computational error is much larger (Fig. 10b), and few flows have a computational error as large as 200 km after 1440

378 hours of integration. In the 3D experiments, the computational errors grew very

379 slowly in the CE (Assum Exp7, Fig. 10c). When the particles moved in the eddy with

380 an integration period of less than 1000 hours, the computational error was always

381 maintained below 5 km. Actually, 85% of the particles can always maintain

382 computational errors smaller than 5 km in the 1440-hour integration when the time

383 step is no more than 60 s (not given). In the AE (Assum Exp8, Fig. 10d), the results

384 are nearly the same. When the time step is smaller than 60 s, the maximum

385 computational error in all particles could be maintained smaller than 25 km over a

386 long integral period (i.e., 2 months). Moreover, more than 85% of particles could

387 maintain computational errors smaller than 5 km. However, when the time step was

388 larger than 300 s, the computational error grew fast and reached values as high as 300

389 km during the 1440-hour integration.

390

391 Compared with the computational errors in the idealized simulation and the realistic

392 simulation, we found that the computational error is much smaller in the realistic

393 simulation during the same integral period of the Lagrangian analysis. The main

394 reason for the smaller computational errors in the realistic simulation analysis than in

395 the idealized simulation analysis is because of the different horizontal resolution. The

396 horizontal resolution of the realistic simulation is five times of that of the idealized

397 simulation. As a result, we suggest that the period of the Lagrangian analysis, which

398 was applied to a 5 km-resolution dataset, could be more than 2 months, whereas we

399 chose a time step smaller than 60 s for the Lagrangian analysis.

400

401 *4.4.2   Current features*

402 We also estimate how current features influence the computational error when the

403 Lagragian analysis is applied to a realistic simulation. In general, the correlation

404 coefficient between the current feature and the growth rate of the computation error

405 increased (Fig. 11) with a larger time step, which is consistent with the conclusion in

406 the idealized simulation. In the downwelling, the correlation coefficient between the

407 divergence (Fig. 11a; vertical velocity shear, Fig. 11b) and the growth rate of the

408 computation error was larger than 0.025 (0.05), and the sign was consistent with the

409 results in the idealized simulation. However, the correlation coefficient between the

410 vertical vorticity and the growth rate of the computation error (Fig. 11c) was 0.01 and

411 the sign was opposite the result in the idealized simulation; thus, we think that the

412 relationship between the vertical vorticity and the growth rate of the computational

413 error was not significant. In the upwelling, the correlation coefficient between the

414 divergence (Fig. 11d; vertical velocity shear, Fig. 11e) and the growth rate of the

415 computation error was more than 0.11 (0.08), which is consistent with the conclusions

416 drawn in the idealized simulation. The correlation coefficient between the vertical

417 vorticity and the growth rate of the computational error (Fig. 11f) was only -0.04. The

418 results are consistent with our previous conclusions.

419

420 The reason that the correlation coefficient is smaller in the realistic simulation is that

421 the sample number is four times larger than that in the idealized eddy. However, the

422 opposite sign in the vertical vorticity analysis indicates that it should be eliminated

423 from our consideration. Based on the results from the idealized simulation and

424 realistic simulation, we found that the growth rate of the computational error is mainly

425 determined by the divergence and vertical velocity shear, which means that the

426 computational error is more likely to increase under a more divergent and stronger

427 vertical diffusive flow.

428

429 **5. Results and Analysis**

430 In this study, we analyzed an idealized mesoscale eddy and performed a realistic

431 simulation of the AE/CE eddy pair off the central Vietnam. In the idealized

432 simulation, a mesoscale eddy was trapped over a seamount and downwelling

433 (upwelling) appeared over (along) the seamount. The downwelling (upwelling)

434 induced positive (negative) vorticity over (along) the seamount, which drove the

435 current to rotate cyclonically (anticyclonically). In the AE/CE eddy pair,

436 downwelling/upwelling appeared inside the anticyclonic/cyclonic eddy since the

437 convergence/divergence appeared at the surface and divergence/convergence

438 appeared in the lower layers. However, by applying the Lagrangian analysis to the

439 realistic eddy-pair, we suggested the readers to be more careful, when select the

440 position to put the tracers. As in the real ocean, the vertical motion is not homogenous

441 inside the eddy, or even be in the opposite direction. Careless selection may lead to

442 wrong eddy structure demonstration.

443

444 Compared with previous studies, we described the eddy structure to a greater extent

445 using a Lagrangian view in several ways.

446

447 In the Lagrangian analysis of the idealized mesoscale eddy, the horizontal current was

448 first demonstrated at the surface and lower layers. The distribution of the particles,

449 with their colors varying over time along the trajectories, demonstrated how the

450 current converged to the center of the eddy at the surface and converged to the

451 upwelling zone in the bottom layer. The convergence at the surface caused the

452 particles to eventually accumulate in a small zone. Thus, the computational error

453 always approached zero in long-term integrations. On the other hand, the

454 computational error was always larger in the bottom layer because the particles

455 diverged rapidly due to the current distribution. In the realistic simulation, the

456 particles converged (diverged) in the upper layer of the AE (CE) and diverged

457 (converged) in the lower layer of the AE (CE). The computational error is always

458 larger in the divergent flow than in the convergent flow, which is consistent with the

459 results of the idealized simulation.

460

461 The most important part of this study is that the 3D structure of the mesoscale eddy

462 was well demonstrated via the Lagrangian analysis. In the idealized mesoscale eddy,

463 we released particles at the surface and tracked their trajectories in the following

464 integration. The particles of different colors in different periods suggested that the

465 current rotated and converged in the horizontal panel and sunk down to lower layers

466 inside the mesoscale eddy. The particles stayed inside the eddy until they reached the

467 bottom and sunk along the seamount to lower layers. We also released particles in

468   lower layers outside the mesoscale eddies. The particles with different colors in

469   different periods suggested that the water in the lower layer compensated for the

470   water being sucked into the eddy via upwelling. However, the results suggested that

471   only the water in the upwelling zone at the bottom layer could move upward and

472   return to the surface. In the dipole pattern, we released the particles in the upper

473   (lower) layer of the AE (CE). The particles converged to the center of the eddy due to

474   the convergent flow; meanwhile, the particles sank (rose) to lower (upper) layers due

475   to the downwelling (upwelling) inside the AE (CE). The particles of different colors

476   in different periods suggested that the vertical motion inside the eddy pair is not

477   horizontally uniform.

478

479   In our realistic simulation, we also found that fluid exchange does not occur between

480   the AE and CE and the AE/CE pairs are isolated by the northeastward jet between

481   them. As a result, the particles cannot move from the CE to AE and vice versa.

482   Actually, when the particles moved out of the eddies, they would move northeastward

483   carried by the boundary jet along the coast of Vietnam.

484

485   We cannot compare the computational errors for the results with different resolutions

486   since we do not have an actual "real value". However, 85% of particles could

487   maintain a computational error below 3 km in the 3D experiments (1 km in the

488   idealized experiments) if we employed a time step of no more than 60 s and even we

489   integrated the information over 1440 hours (60 days). If the time step is no more than

490   60 s and the integral period is shorter than 500 hours, all the particles can maintain

491   computational errors at an acceptable value (i.e., 1 km). However, when the time step

492   is larger than 300 s, the computational error grows significantly in a short period,

493   which indicates that the trajectories are unconvincing.

494

495   Further analysis suggested that the growth rate of the computational error was related

496   to divergence and vertical velocity shear. As the divergence (vertical velocity shear)

497   increased, the computational error increased. This relationship was more significant

498   with larger time steps. However, the growth rate of the computational error was not as

499   sensitive to the current speed or vertical vorticity in this study.

500

501   The purpose of the study was to demonstrate the 3D structure of the mesoscale eddy

502   from a Lagrangian perspective, and we employed both an idealized simulation and a

503   realistic simulation. To simplify this analysis, we assumed that the eddy was constant,

504   which is unlikely to be realistic. However, we focused on the Lagrangian trajectories

505   and computational error growth rate, which were both well presented in this study.

506   Additionally, we demonstrated the relative independence of Vietnam dipoles via the

507   Lagrangian analysis.

508

509   Because the Lagrangian analysis could adequately describe the structures of the

510   mesoscale eddies, which typically have greater speeds and larger variations than usual

511   currents, we could confidently use the Lagrangian analysis to simulate the trajectories

512   of the particles in a predicted current with a suitable time step and total integral

513   period. The use of this Lagrangian calculation tool in mesoscale current simulations

514   will be studied further in our future work.

515

520

References

Adams, K.A., Hosegood, P., Taylor, J.R., Sallee, J.B., Bachman, S., Torres, R., and Stamper, M., 2017, Frontal Circulation and Submesoscale Variability during the Formation of a Southern Ocean Mesoscale Eddy, J. Phys. Oceanogr., 47, 1737-1753.

Chu, X., Xue, H., Qi, Y., Chen, G., Mao, Q., Wang, D., and Chai, F., 2014, An exceptional anticyclonic eddy in the South China Sea in 2010, J. Geophys. Res., 119, 881-896.

Dai, H., Cui, J. and Yu, J., 2017. Revisiting mesoscale eddy genesis mechanism of nonlinear advection in a marginal ice zone. Acta Oceanol. Sin., 2017, 11, 14-20.

Dong, C., X. Lin, Y. Liu, F. Nencioli, Y. Chao, Y. Guan, D. Chen, T. Dickey, and J. C. McWilliams, 2012, Three-dimensional oceanic eddy analysis in the Southern California Bight from a numerical product, J. Geophys. Res., 117, 881-896.

Döös, K., J. Nycander, and A.C. Coward, 2008, Lagrangian decomposition of the Deacon Cell, J. Geophy. Res., 113, C07028.

Fang, W., Fang, G., Shi, P., et al. 2002. Seasonal structures of upper layer circulation in the southern South China Sea from in situ observations. J. Geophys. Res. Oceans, 107, 23-1-23-12.

Gula, J., Molemaker, M.J. and Mcwilliams, J. C., 2016. Topographic generation of submesoscale centrifugal instability and energy dissipation. Nature Communications 7: 12811.

Gula, J., Molemaker, M.J. and Mcwilliams, J.C., 2015. Topographic vorticity generation, submesoscale instability and vortex street formation in the Gulf Stream. Geophys Res. Lett., 42(10): 4054-4062.

Häkkinen S. 1986. Coupled ice-ocean dynamics in the marginal ice zones: Upwelling/downwelling and eddy generation. J. Geophys. Res. Oceans, 91(C1): 819-832.

Johannessen, J.A., O.M. Johannessen, E. Svendsen, R. Shuchman, T. Manley, W.J. Campbell, E.G. Josberger, S. Sandven, J.C. Gascard, T. Olaussen, K. Davidson, and J. van Leer, 1987, Mesoscale eddies in the Fram Strait marginal ice zone during the 1983 and 1984 Marginal Ice Zone Experiments, J. Geophys. Res., 92, 6754-6772.

Kjellsson, J. and K. Döös, 2012, Lagrangian decomposition of the Hadley and Ferrel cells, Geophys. Res. Lett., 39, L15807.

Kuo, N., Zheng, Q., Ho, C., 2000. Satellite observation of upwelling along the western coast of the South China Sea. Remote Sensing of Environment, 74(3): 463-470.

Lemariè, F., J. Kurian, A.F. Shchepetkin, M.J. Molemaker, F. Colas, and J.C. McWilliams, 2012, Are there inescapable issues prohibiting the use of terrain-following coordinates in climate models, Ocean Model., 42, 57-79.

Liu, A. K., Hakkinen, S. and Peng, C.Y., 1993. Wave effects on ocean-ice interaction in the marginal ice zone. J. Geophys. Res. Oceans, 98(C6): 10025-10036.

Lin, X., C. Dong, and K. Chen, 2018, Cross-basin particle transport by a warm eddy southwest of Taiwan Island, J. Tro. Oceanogr., 37, 9-18.

McWilliams, J.C., 2016, Submesoscale currents in the ocean. Proceedings Mathematical Physical & Engineering Sciences 472(2189): 20160117.

Moore, A.M. , H.G., Arango, G., Broquet, C., Edwards, M., Veneziani, B., Powell, D., Foley, J.D., Doyle, D., Costa, and P., Robinson, 2011, The Regional Ocean Modeling System (ROMS) 4-dimensional variational data assimilation systems: Part III – Observation impact and observation sensitivity in the California Current System, Progress in Oceanography, 91(1): 74-94.

Manucharyan, G.E., and Timmermans, M.L,, 2013. Generation and Separation of Mesoscale Eddies from Surface Ocean Fronts. J. Phys. Oceanogr. 43(12): 2545–2562.

Manucharyan, G.E. and Thompson, A.F., 2017. Submesoscale Sea Ice-Ocean Interactions in Marginal Ice Zones. J. Geophys. Res. Oceans, 122(12): 9455-9475.

Nakamura, T., Matthews, J.P., Awaji, T., et al. 2012. Submesoscale eddies near the Kuril Straits: Asymmetric generation of clockwise and counterclockwise eddies by barotropic tidal flow. J. Geophys. Res. Oceans. 117(C12): C12014.

Okubo, A., 1970, Horizontal dispersion of floatable particles in the vicinity of velocity singularities such as convergences, Deep Sea Res. PartI., 17, 445-454.

Sebille, E., S. M. Griffies, R. Abernathey, T. P. Adams, P. Berloff, A. Biastoch, B. Blanke, E. P. Chassignet, Y. Cheng, C. J. Cotter, E. Deleersnijder, K. Döös, H. F.

581   Drake, S. Drijfhout, S. F. Gary, A. W. Heemink, J. Kjellsson, I. M. Koszalka, M.

582   Lange, C. Lique, G. A. MacGilchrist, R. Marsh, C. G. M. Adame, R. McAdam, F.

583   Nencioli, C. B. Paris, M. D. Piggott, J. A. Polton, S. Rühs, S. H.A.M. Shah, Ma. D.

584   Thomas, J. Wang, P. J. Wolfram, L. Zanna, J. D. Zika, 2018, Lagrangian ocean

585   analysis: Fundamentals and practices, Ocean Model., 121, 49-75.

586 Shchepetkin, A.F. and J. C. McWilliams, 2005, The Regional Oceanic Modeling

587   System (ROMS): A split-explicit, free-surface, topography-following-coordinate

588   oceanic model, Ocean Model., 9, 347-404.

589 Torres, T.S., Klein, P., Menemenlis, D., Qiu, B., Su, Z., Wang, J., Chen, S., Fu, L., 2018.

590   Partitioning ocean motions into balanced motions and internal gravity waves: a

591   modeling study in anticipation of future Space missions. J. Geophys. Res. 123,

592   8085-8105.

593 Wang, G., Chen D. and Su, J., 2006, Generation and life cycle of the dipole in the South

594   China Sea summer circulation, J. Geophys. Res., 111(C6): C06002.

595 Weissa, J., 1991, The dynamics of enstrophy transfer in two-dimensional

596   hydrodynamics, Phys. D., 48, 273-294.

597 Xie, S., Xie, Q., Wang, D., Liu, W.T., 2003, Summer upwelling in the South China Sea

598   and its role in regional climate variations. J. Geophys. Res., 108(C8), DOI:

599   10.1029/2003JC001867

600 Zhang, X., Dai, H., Zhao, J., Yin, H., 2019, Generation mechanism of an observed

601   submesoscale eddy in the Chukchi Sea. Deep Sea Res Part I, in press, DOI:

602   https://doi.org/10.1016/j.dsr.2019.04.015

603

Figure Captions
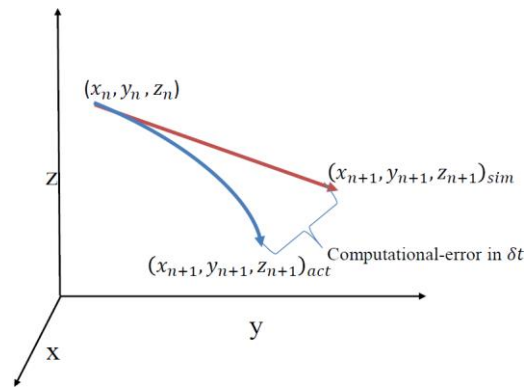
606 Fig.1. Schematic figure of the trajectory during the (n+1)th timestep: ()$_{act}$ represents the

607 particle's actual location after the (n+1)th time step, while ()$_{sim}$ represents the particle's

608 location calculated by the Lagrangian calculation tool.

610

611
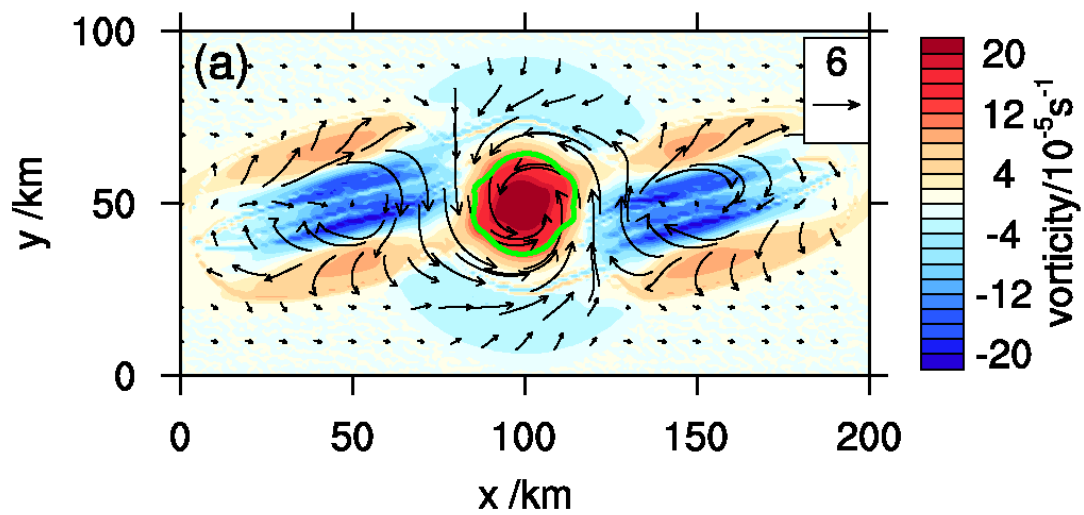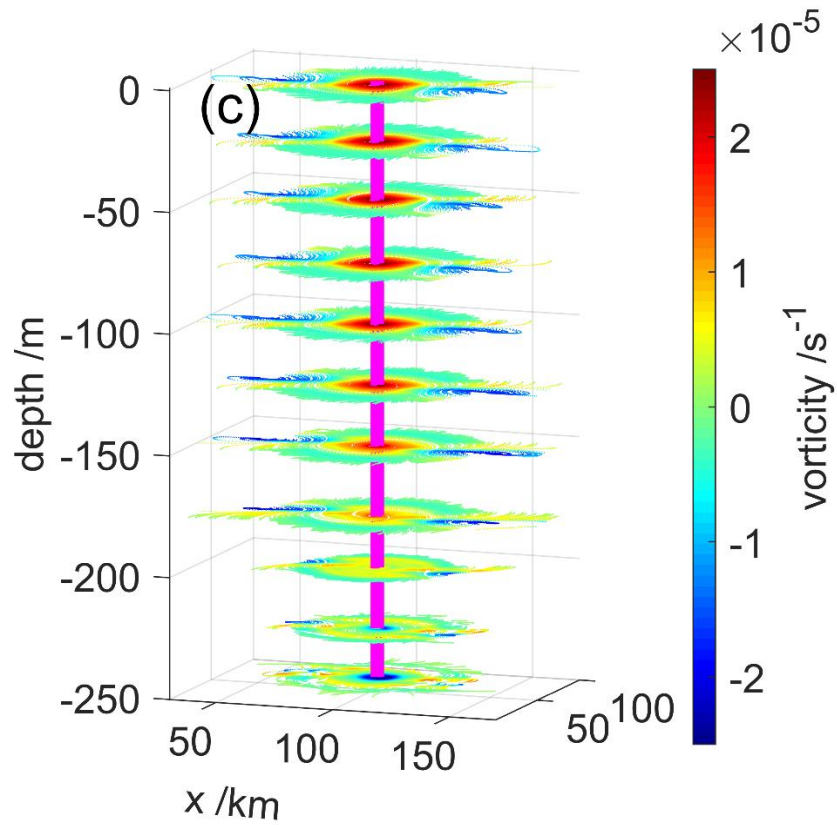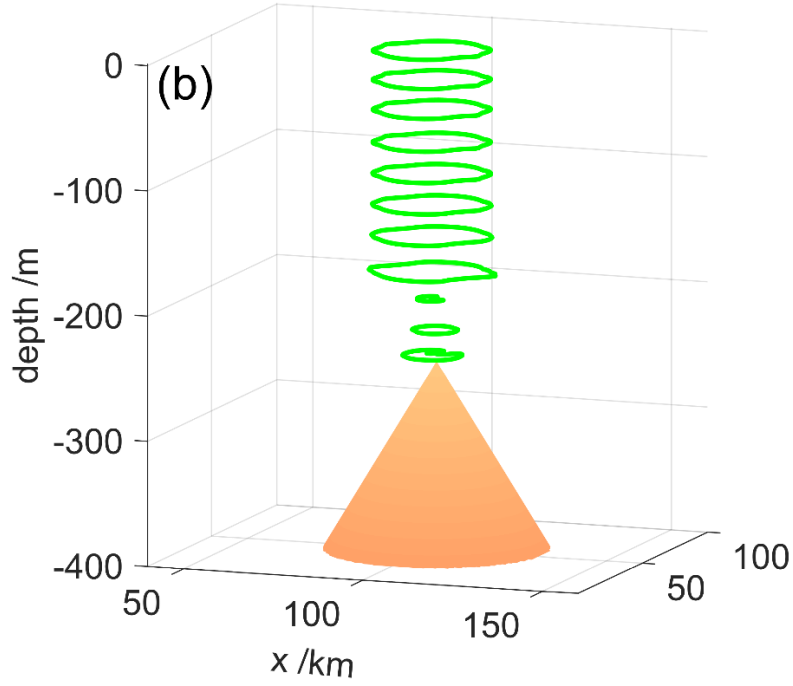
Fig.2. (a) The distributions of the surface current (vectors, unit: cm/s) and vertical vorticity (shading, unit: 10^{-5} s^{-1}) are shown in (a). The eddy boundary is shown with green contours at different layers in (b). The vertical vorticities in different layers are shown in (c), unit: 10^{-5} s^{-1}.

616
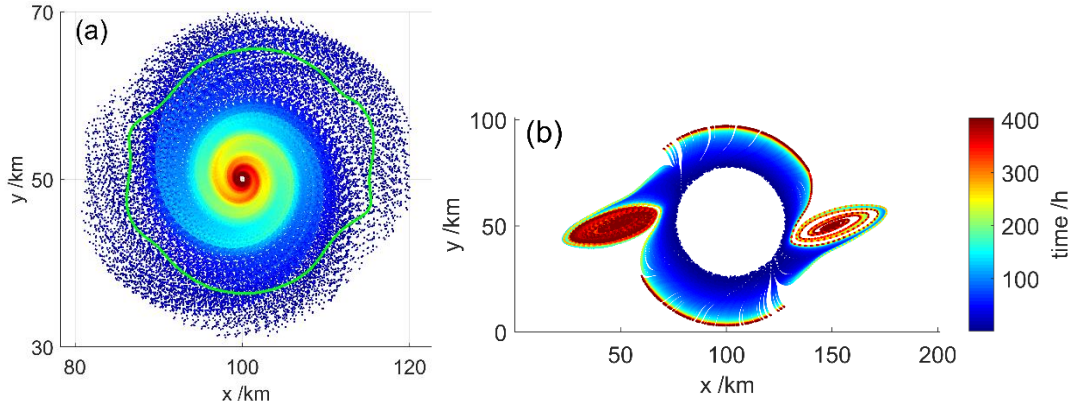
Fig.3. Horizontal movements of the particles (dots) and eddy boundary (green line) in

the surface and bottom layers are shown in (a) and (b), respectively.

619

620
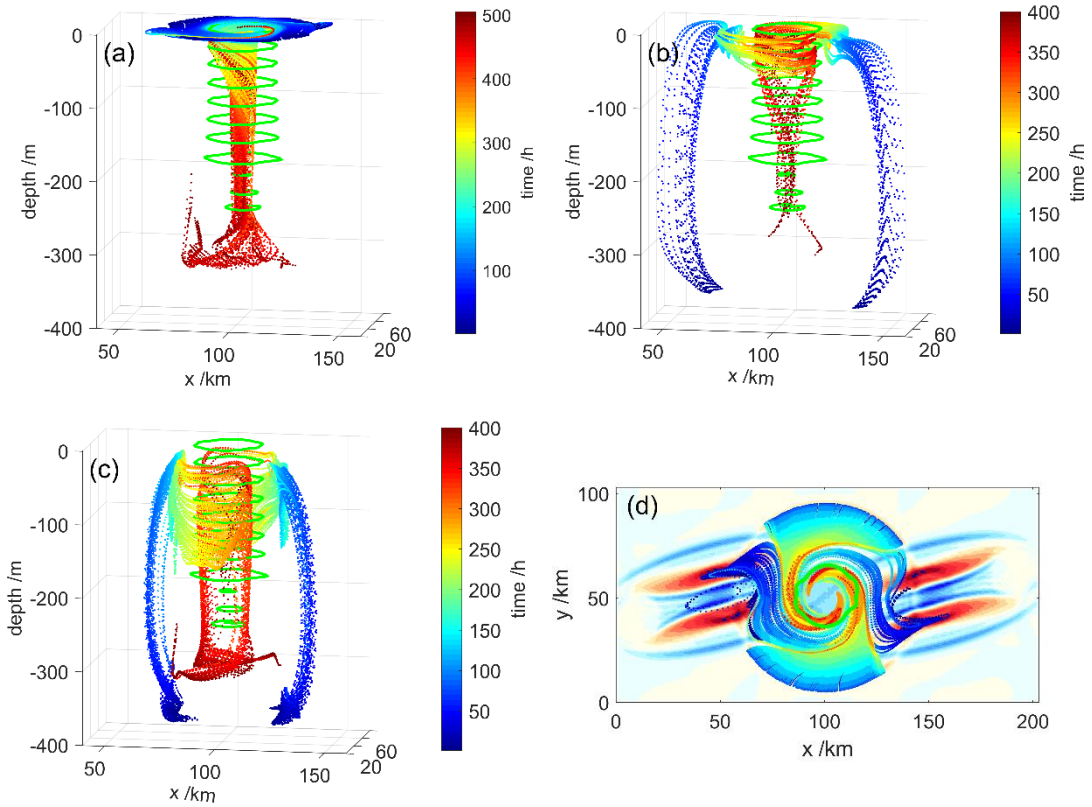
621 Fig.4. Particles released outside the surface eddy boundary (Exp3) and their tracked

622 trajectories are shown in (a). Particles released in the upwelling zone at the bottom layer

623 (Exp4) and their tracked trajectories are shown in (b). Particles released at the bottom

624 of the seamount (Exp5) and their tracked trajectories are shown in (c). Vertical view of

625 (b) and the depth-averaged vertical velocity (shading, unit: 0.1 mm s-1) are shown in

626 (d).

627

628
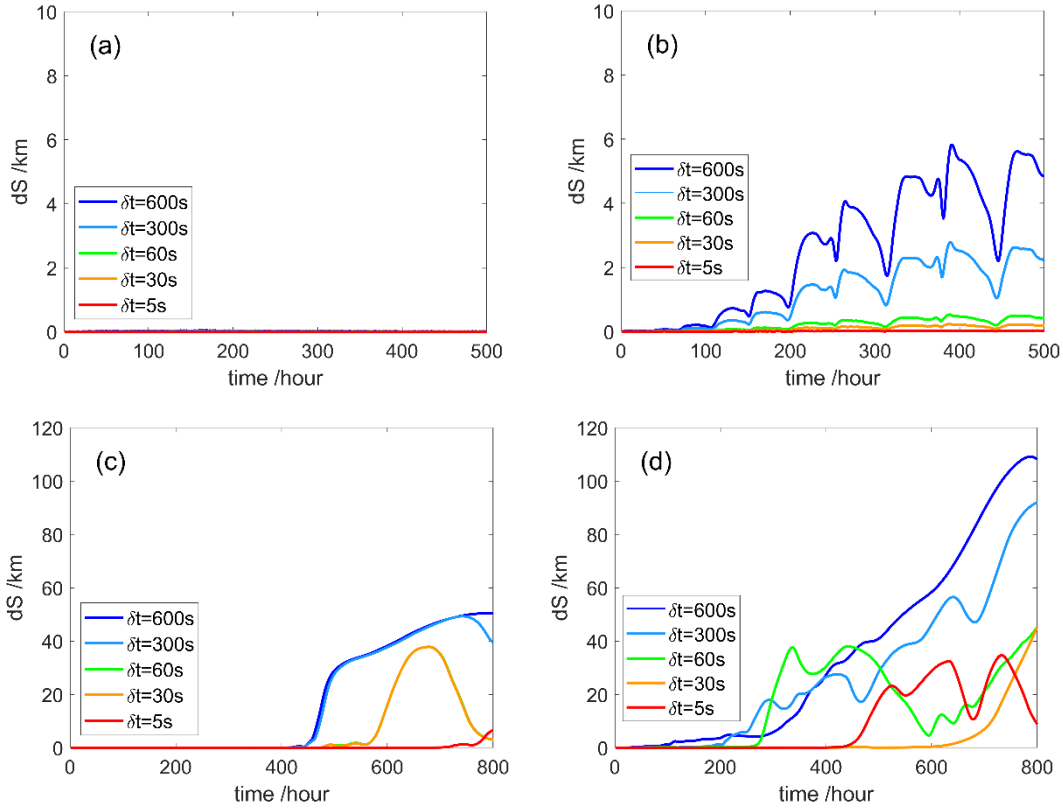
Fig.5. Maximum computational error estimates obtained with different time steps when the particles moved in the surface (Exp1 and Assum Exp1) and bottom layers (Exp2 and Assum Exp2) in the 2D experiments are shown in (a) and (b), unit: km. Maximum computational error estimates obtained with different time steps when the particles moved in the downwelling (Exp3 and Assum Exp3) and upwelling (Exp4, Assum Exp4, Exp5 and Assum Exp5) in 3D experiments are shown in (c) and (d), unit: km. The blue, cyan, green, orange, and red lines indicate the computational errors obtained using the time steps of 600 s, 300 s, 60 s, 30 s and 5 s, respectively.


637

638

639

640
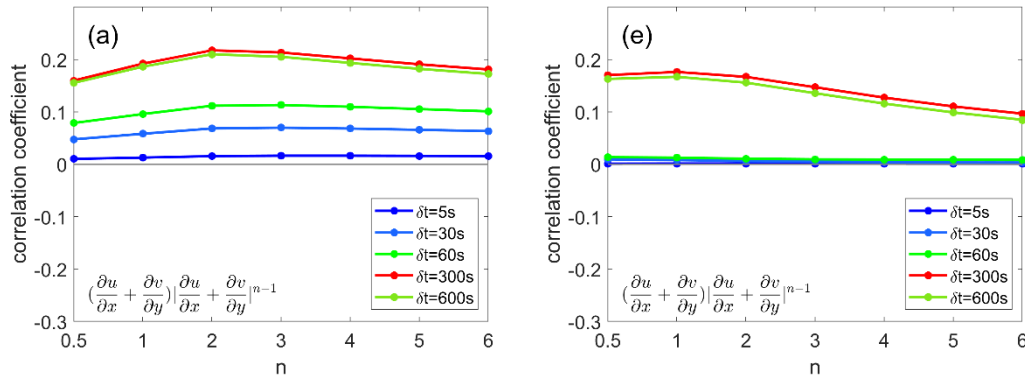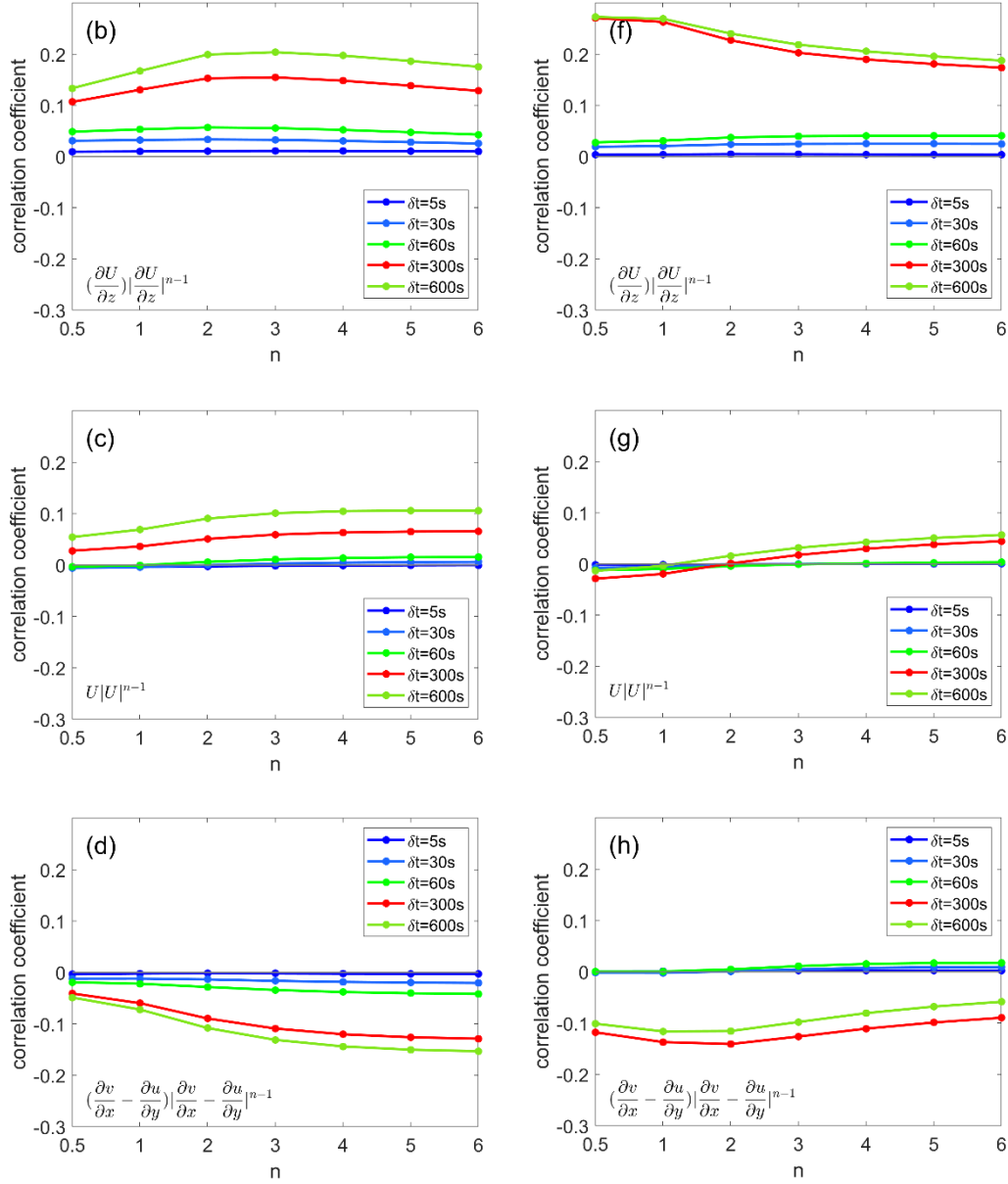
641 Fig.6. Correlation coefficients between the growth rate of the computational error and

642 the current features in the downwelling are estimated. Current features include the (a)

643 divergence ($\frac{\partial u}{\partial x} + \frac{\partial v}{\partial y}$), (b) vertical shear ($|\frac{\partial \vec{V}}{\partial z}| = |\frac{\partial u}{\partial z}\vec{i} + \frac{\partial v}{\partial z}\vec{j}|$), (c) current speed

644 ($|\vec{V}| = |u\vec{i} + v\vec{j}|$), and (d) vertical vorticity ($\frac{\partial v}{\partial x} - \frac{\partial u}{\partial y}$), and we also consider the nth

645 power of the variable (n=0.5, 1, 2, 3, 4, 5, 6; however, we always kept the sign of the

646 variable). (e), (f), (g), (h) Same as (a), (b), (c), (d) but are correlation coefficients in the

647 upwelling. The blue, cyan, green, orange, and red lines indicate the correlation

648 coefficient obtained using the time steps of 600 s, 300 s, 60 s, 30 s and 5 s, respectively.

649

650
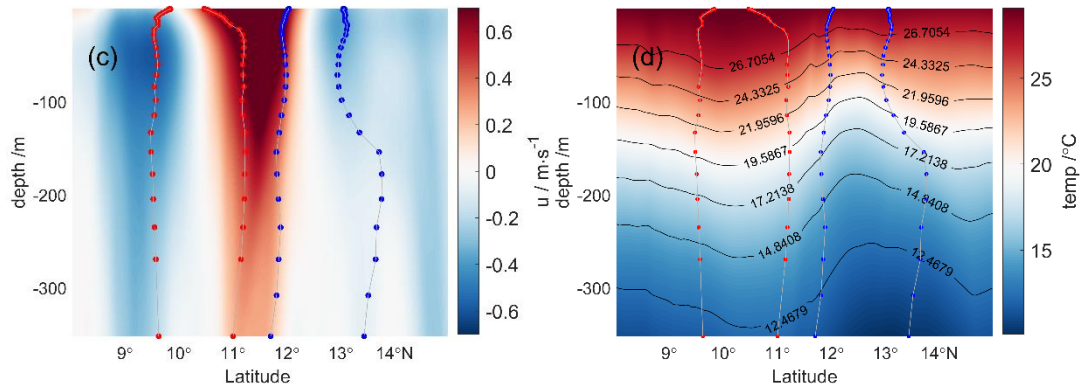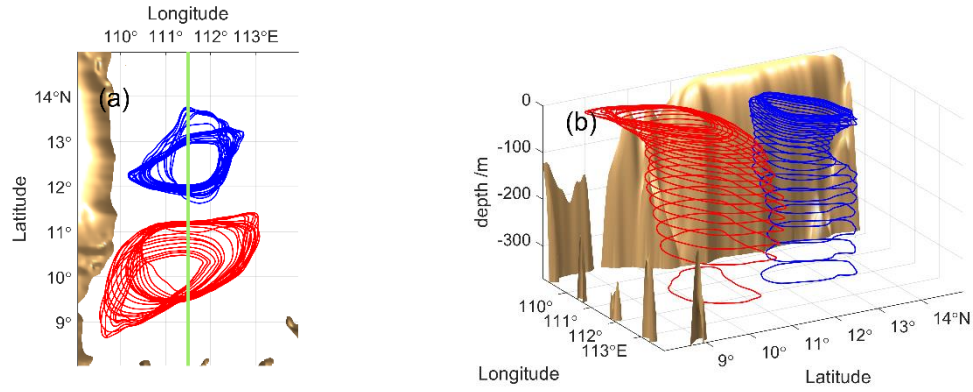
Fig.7. Vertical view of the eddy boundary of AE (red line) and CE (blue line) in each layer are shown in (a), with a green line nearly across the centers of the two eddies. The 3D structure of the eddy boundary is also shown in (b). The orange shading indicates the topography. Along the green line in (a), the vertical profile of the velocity in the meridional direction (unit: m/s) and the temperature (unit: °C) are shown as shading in (c) and (d), respectively, while the red and blue dot lines represent the eddy boundary in each layer. Selected isotherms are also presented as contours in (d), unit: °C.

658
659
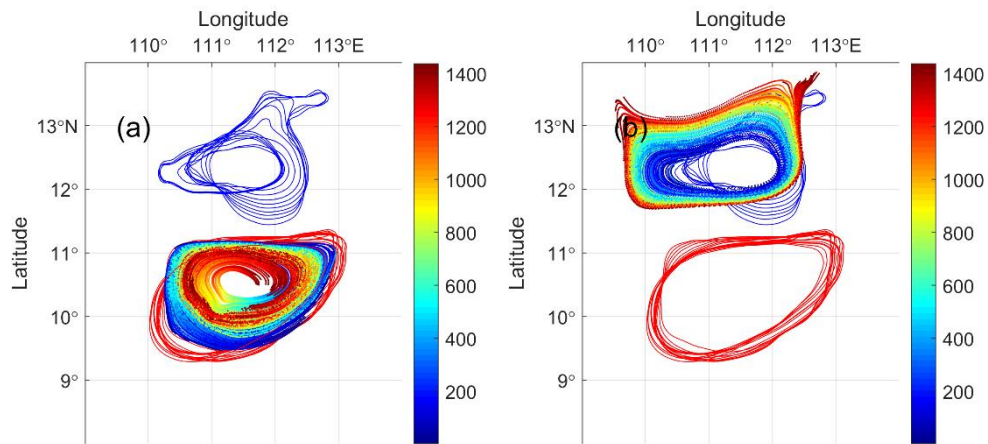
660 Fig.8. Particles released at z=-28 m in Exp6; the trajectories of the particles in (a) AE

661 and (b) CE are tracked by the dots, whose colors change with time. The eddy boundary

662 in each layer of AE (red line) and CE (blue line) on September 13, 2013 are shown.

663 Unit: hour.

664
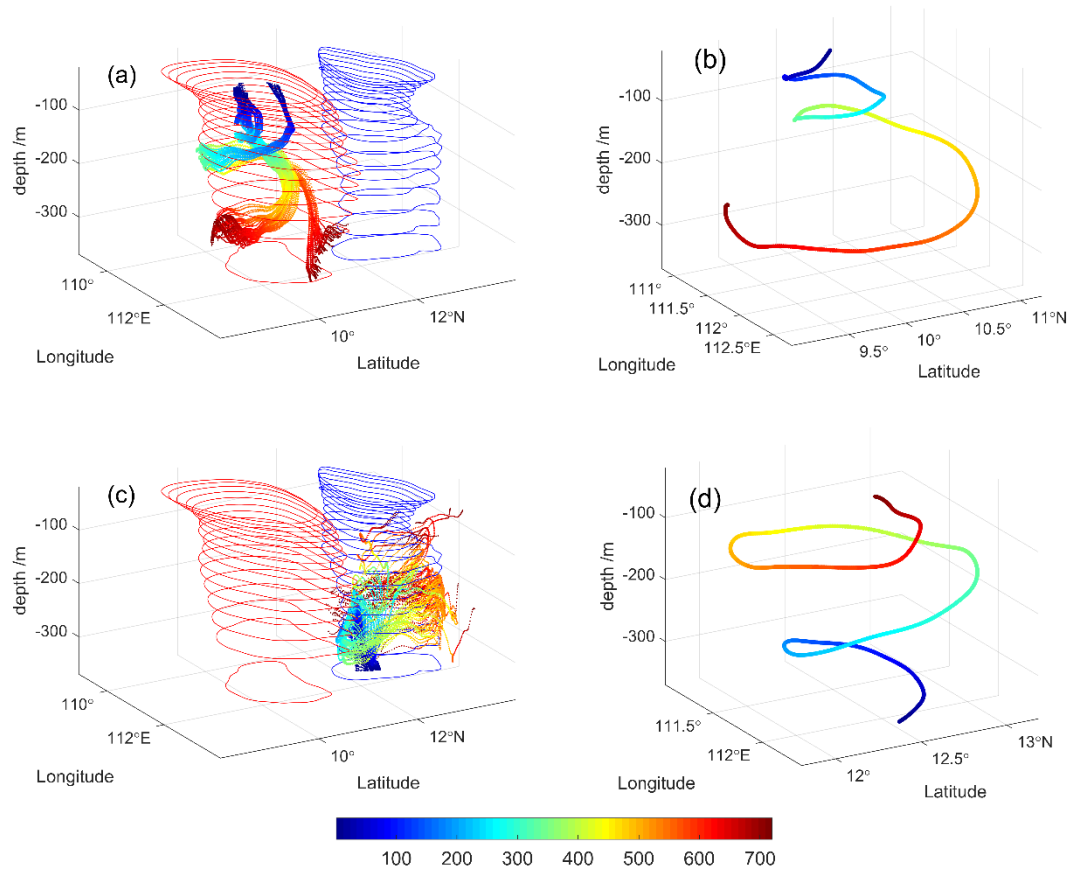
665 Fig.9. Particles released at z=-28 m /-352 m inside AE/CE in Exp7/Exp8 the trajectories

666 of the particles are tracked by dots in (a)/(c), and the color indicates the integration

667 period. A typical trajectory in AE or CE is selected and demonstrated in (b) and (d),

668 respectively. Unit: hour.

669

670

671
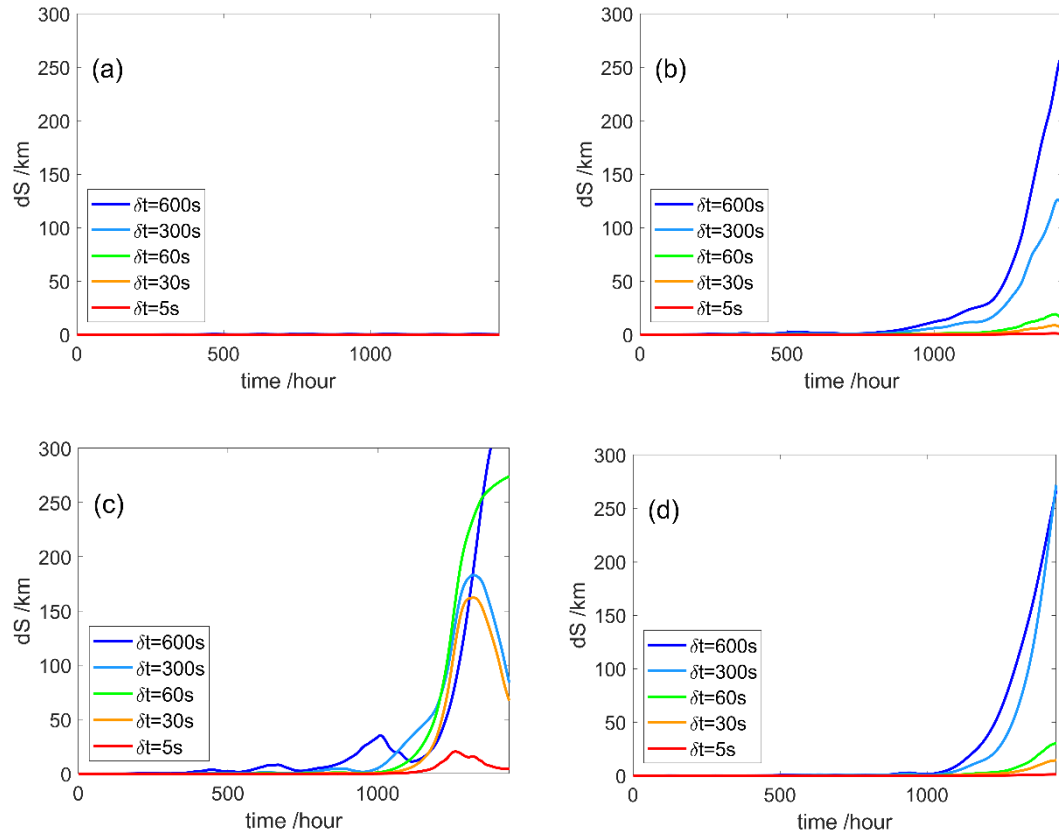
Fig.10. Maximum computational error in (a) and (b) are estimated from particles in the CE and AE in Exp6 and Assum Exp6, respectively. The maximum computational error in (c) is estimated from particles in Assum Exp7. The maximum computational error in (d) is estimated from particles in Assum Exp8. Unit: km. The blue, cyan, green, orange, and red lines indicate the errorobtained using the time steps of 600 s, 300 s, 60 s, 30 s and 5 s, respectively.
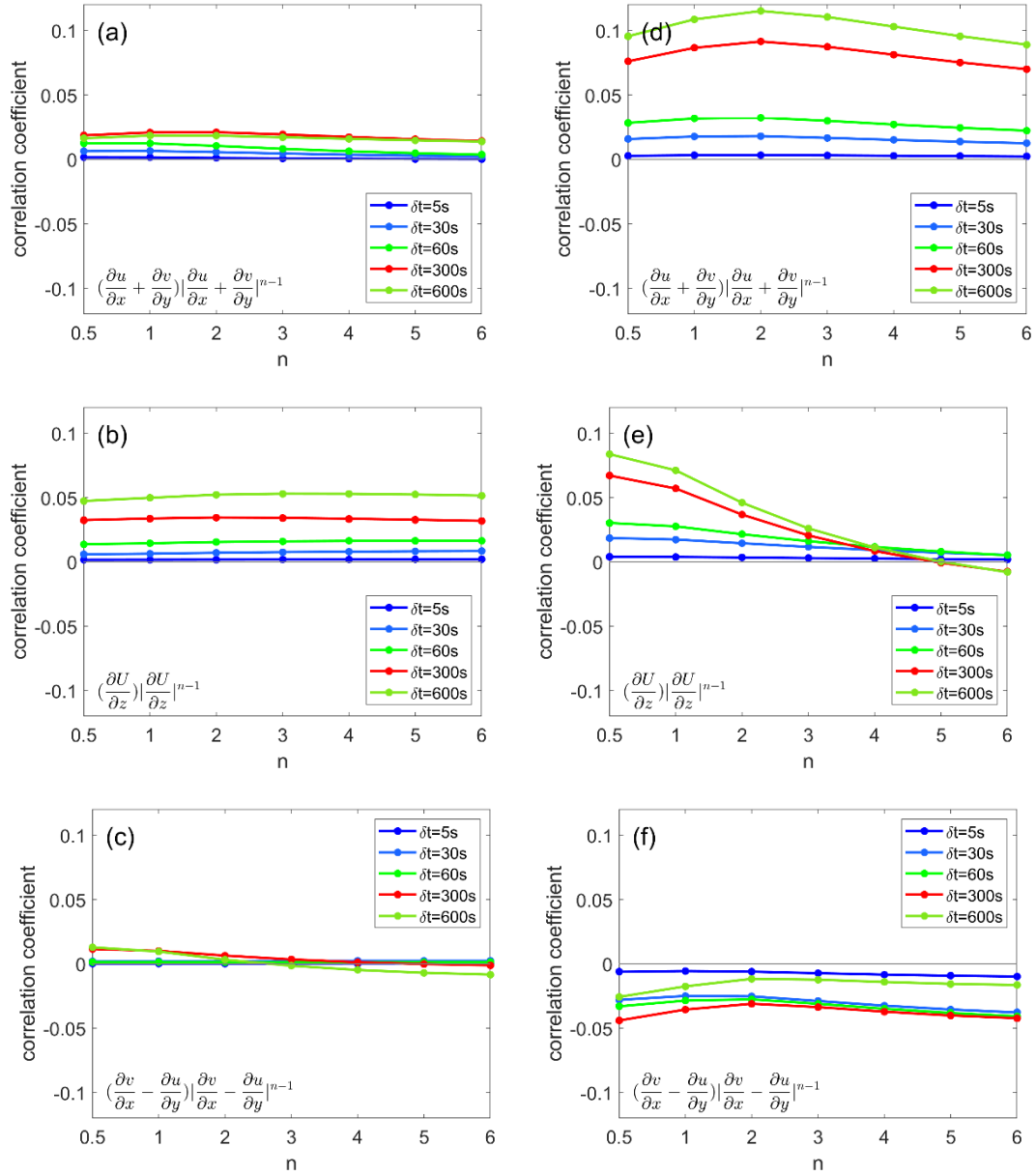
679

680

681

682 Fig.11. Same as Figure 6 but the current speed is neglected. (a) (b) (c) Correlations

683 coefficient estimated from Assum Exp7; (d) (e) (f) correlation coefficients estimated

684 from Assum Exp8. The blue, cyan, green, orange, and red lines indicate the correlation

685 coefficient obtained using the time steps of 600 s, 300 s, 60 s, 30 s and 5 s, respectively.

686

687

688

689

690

691

Appendix A. Mesoscale eddy simulation and analysis

Previous studies suggested there are three mesoscale eddy genesis mechanisms generally. The first one is the topography variations in the bottom, which increases the vorticity and form mesoscale eddies via potential vorticity conservation(Gula et al. 2015,2016). The second one is unstable energy induced by barotropic and / or baroclinic instability can help small scale turbulence grow into mesoscale eddies(Nakamura et al., 2012; Manucharyan and Timmermans 2013; Manucharyan and Thompson 2017). The third eddy genesis mechanism is in the ice zone, as the momentum transferred from the wind is more efficiently via sea ice than to the ocean directly, there is velocity shear at the ice boundary, which can be increased and form mesoscale eddies by nonlinear advection of the current(Häkkinen 1986; Liu et al., 1993; Dai et al., 2017).

A mesoscale eddy generated by the first mechanism can be maintained in the same region. Mesoscale eddies generated by the second mechanism form quickly but always move following the jet or the front. A great number of the eddies are produced at the same time and can hardly be separated from each other. Mesoscale eddies produced by the third eddy genesis mechanism are generally very weak, especially in deep water. As a result, we employ the second mechanism to generate mesoscale eddies with a numerical ocean model and use topography to maintain the eddy in the same region.

A.1 Model and experiment settings

The numerical ocean model used in this study is the Regional Oceanic Modeling System (ROMS), which solves 3D hydrostatic primitive equations (Shchepetkin and McWilliams, 2005) with vertical hybrid z-sigma coordinates (Lemariè et al., 2012). The theoretical framework of this model is written as follows:

$$\frac{\partial \vec{u}}{\partial t} + (\vec{u} \cdot \nabla_\perp)\vec{u} + \vec{w}\frac{\partial \vec{u}}{\partial z} = -\nabla_\perp \Phi - f\vec{z} \times \vec{u} + \vec{\tau}_{aw} \qquad (1)$$

$$\frac{\partial \Phi}{\partial z} + \frac{g\rho_w}{\rho_0} = -\frac{\partial \Gamma}{\partial z} \qquad (2)$$

$$\nabla_\perp \cdot \vec{u} + \frac{\partial w}{\partial z} = 0 \qquad (3)$$

$$\frac{\partial c}{\partial t} + (\vec{u} \cdot \nabla_\perp)c + w\frac{\partial c}{\partial z} = D^c + Q^c \qquad (4)$$

where $\vec{v} = (u, v)$ is the current velocity vector; u, v, and w are the current velocities in the x, y and z directions, respectively; and Φ is the sea surface potential function, and f is the Coriolis parameter. In this case, f=0.0001 s-1. In addition, c is the tracer (i.e., temperature, salinity), Dc represents the tracer diffusion, Qc is the source of the tracer. τaw is the wind stress exerted on the current, and ρw and ρ0 are the water density and water reference density, respectively.

The model is configured on a 200 km×100 km domain with a horizontal resolution of 1 km. There are 40 grid levels in the vertical direction, spanning a total depth of 400 m. There are north-south periodic boundaries and east-west periodic boundaries. In the model run, the reference water density is 1027.5 kg·m-3. A front was located along the seamount in the initial field (Fig. A1a), and another two fronts appeared as ellipses close to the seamount (Fig. A1b). In addition, the initial velocity fields are set to zero. A constant and uniform wind (1.8 m/s, Fig. A1c, vectors) is applied to the entire domain, while a seamount is placed at the center of the modeled region, with a total height of 150 m and a topography gradient of 5 m/km (Fig. A1c, shading). The model is integrated for 3 model days, although the result at the end of the 6th hour is used for more beautiful eddy structure (We aim to introduce a better method of presenting the eddy structure instead of discussing the eddy evolution).

A.2 Mesoscale eddy analysis

The fronts contained substantial amounts of available potential energy. However, they existed in an unstable state and slumped over a short time. After 6 hours of integration, the front over the seamount diminished significantly (Fig. A2a). Two fronts near the seamount diminished and were separated into a few segments (Fig. A2b). When the density over the seamount was larger than that of the surrounding water, downwelling occurred (Fig. A2c). Close to the seamount, lighter and denser water corresponded to upwelling and downwelling, respectively (Fig. A2c). When the fronts slumped due to

749 gravity, the available potential energy was converted into a current, which helped the
750 turbulence grow into a mesoscale eddy. The primary eddy grew over the seamount and
751 was maintained over the seamount. The downwelling determined the positive vorticity
752 over the seamount, and the current rotated cyclonically (Fig. A2d).
753
754 In a 3D structure, the downwelling over the seamount and the upwelling along the
755 seamount dominated the entire column (Fig. A3a, b). On the eastern and western sides
756 of the seamount, mixing occurred with upwelling and downwelling. Due to the
757 distribution of upwelling and downwelling, a convergence formed at the bottom of the
758 seamount (Fig. A3c, x=75 km and x=125 km) and a divergence formed at the bottom
759 of the downwelling (Fig. A3c, x=50 km and x=150 km). Due to vertical convection, the
760 relative vorticity was positive (negative) when there was downwelling (upwelling).
761 Thus, du/dy is negative (positive) over (along) the seamount (Fig. A3d). In contrast,
762 dv/dx is positive (negative) over (along) the seamount (Fig. A3e). The currents mainly
763 flow over the seamount in the x direction, as v is small in the section x=100 km (Fig.
764 A3f). Because baroclinic instability was dominant in this study, the potential vorticity
765 conservation law was invalid.
766
767 **Appendix B. Eddy pair in the South China Sea**
768 **B.1 Experiment settings**
769 The west part of the SCS (106°E~116°E, 4°N~18°N) was simulated by ROMS
770 (University of Rochester version), with a resolution of 1/20° in the horizontal
771 direction and 48 levels in the vertical direction. To improve the accuracy of our
772 simulation, a strong constraint 4D-Var (I4DVAR) scheme (Moore et al., 2011) was
773 implemented into the ROMS to finish data assimilation with satellite observations
774 (sea surface temperature (SST) and sea level anomaly (SLA)) and in situ
775 temperature/salinity (T/S) profile (Argo, Conductivity-Temperature-Depth recorder
776 (CTD) and etc.). The gridded bathymetric data from GEBCO08
777 (https://www.gebco.net/data_and_products/gridded_bathymetry_data/) with a
778 minimum depth of 10 m and a maximum depth of 5500 m were used for the

779   topography. Three-hourly wind (ERA-Interim,

780   https://www.ecmwf.int/en/forecasts/datasets/reanalysis-datasets/era-interim) from the

781   European Centre for Medium-Range Weather Forecasts (ECMWF) was used as wind

782   forcing. We employ open boundary condition in each boundary. At the boundary, the

783   current was relaxed to a climate status, which is satisfied with monthly reanalysis data

784   (The Simple Ocean Data Assimilation, SODA 3.3.1,

785   https://www.atmos.umd.edu/~ocean/index_files/soda3.3.1_mn_download.htm). Along

786   with model integration, Satellite SST from the Advanced Very High-Resolution

787   Radiometer (AVHRR, ftp://eclipse.ncdc.noaa.gov), SLA from the Satellite derived

788   Sea Surface Height above Geoid (AVISO, http://www.aviso.oceanobs.com/duacs/), in

789   situ T/S profile data from EN4.2.1 (http://hadobs.metoffice.com/en4/download.html)

790   were assimilated and input into the ocean model every 4 days. The model was

791   integrated for 9 months, which started on 1 January, 2013, while we employed the

792   results from September 2013.

793

794   **B.2 Three-dimensional structure of the eddy pair**

795   In our simulation, the dipole structure of the eddy pair appeared off the central Vietnam

796   during September, 2013 (Fig. B1a), which is consistent with the observations (Fig. B1b).

797   We also employ a trajectory of Argo No. 5904191 (Fig. B1c, green line) at the layer of

798   -1200 m through the whole September. The eddy captured by the Argo can also be found

799   in our simulation (Fig. B1c, vector), although the Argo located more to the west,

800   because of the large horizontal decorrelation scale used in the assimilation setting. Back

801   to the current field, several eddies (not given) were observed with the eddy boundary

802   definition. However, in this simulation, the boundary defined with vector geometry

803   method (Nencioli et al., 2010) proposed by Dong (Dong et al., 2012) can better capture

804   the eddy features than the OW method. The results suggested that only the primary

805   AE/CE pair always stays in the region of [109E-114E, 8N-15N] through the whole of

806   September 2013.

807

808   The outline of the AE/CE pair (Fig. B2) suggested that the radius of the AE (Fig. B2a,

809   red line) expanded to as much as 131 km (average radius is 116 km), which is larger

810   than the radius of the CE (110 km and 88 km for the maximum and average radius,

811   respectively. Fig. B2a, blue line), because the positive potential vorticity increased

812   when the flow climbed over the seamounts by the potential vorticity conservation law.

813   However, the CE (Fig. B2b blue line) extended to deeper layers (1000 m) than the AE

814   (350 m). The AE/CE pair on September 13, 2013 was chosen for better analysis since

815   the eddies appeared as quasi-cylinders, which made the analysis simpler.

816

817   In the profile (x=113E, Fig. B3a), eastward flow occurred in the south(north) part of

818   the CE(AE), while westward flow (Fig. B3b) occurred in the north (south) part of the

819   CE (AE), which indicated that the current rotated cyclonically (anticyclonically) in the

820   CE (AE). The zonal flow, which has a maximum velocity as high as 1.4 m/s, was nearly

821   uniform in each layer above 350 m. As a result, downwelling (upwelling, Fig. B3c)

822   occurred in the AE (CE), although the vertical motion was not consistent inside the

823   eddies. Disturbed by the vertical flow, the isotherms (Fig. B3d) sank (lifted) in the AE

824   (CE).

825

826   The profile of the eddies were separately checked (Fig. B4a, b). As the current rotated

827   anticyclonically in the AE, northward and southward flows occurred in the west and

828   east part of AE (Fig. B4c), whereas southward and northward flows occurred in the

829   west and east part of CE (Fig. B4d). For the vertical motion, the results were consistent

830   with the meridional profile. There was approximately uniform downwelling (Fig. B4e,

831   upwelling, Fig. B4f) inside the AE (CE), although the downwelling inside the AE is

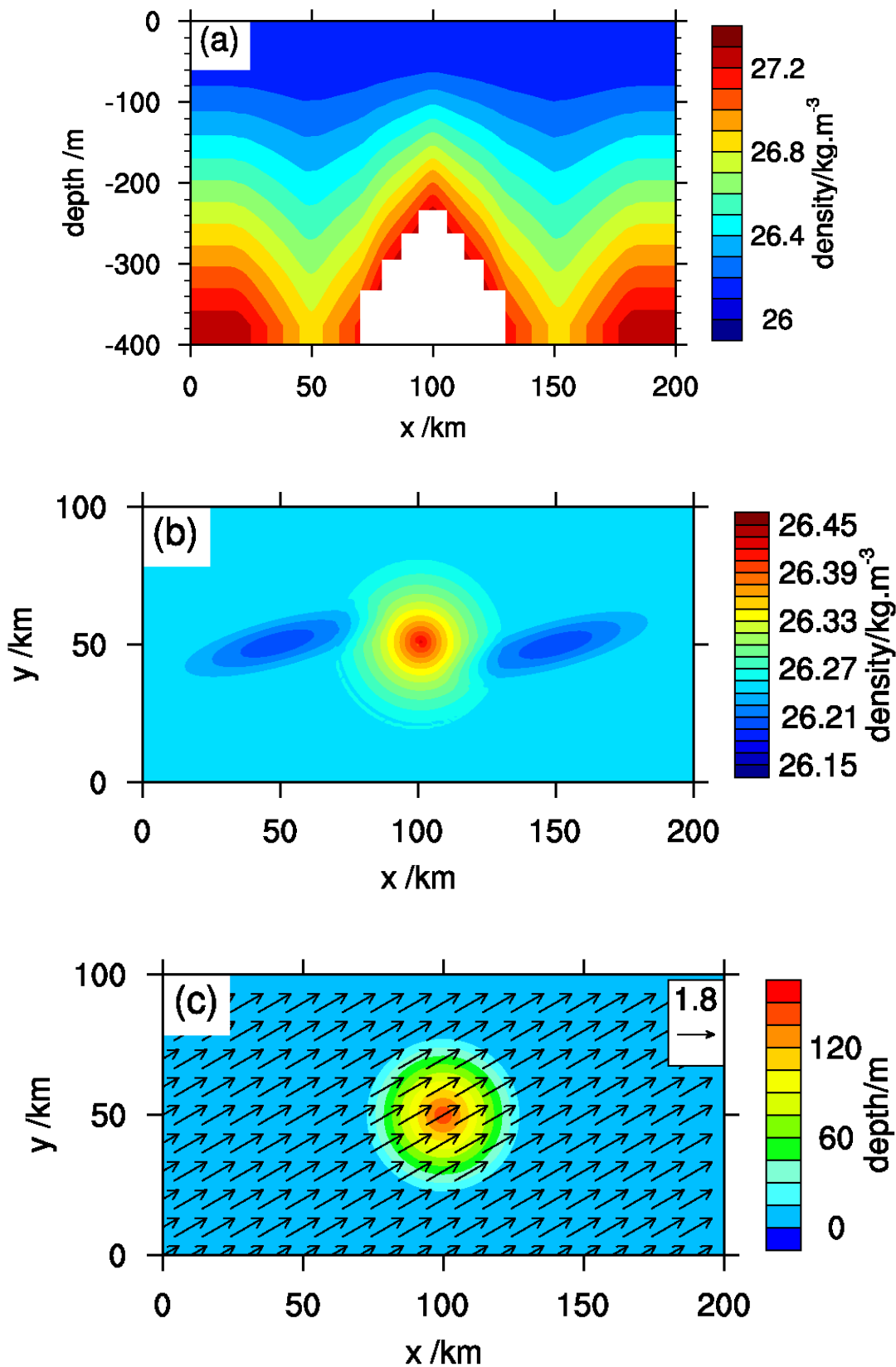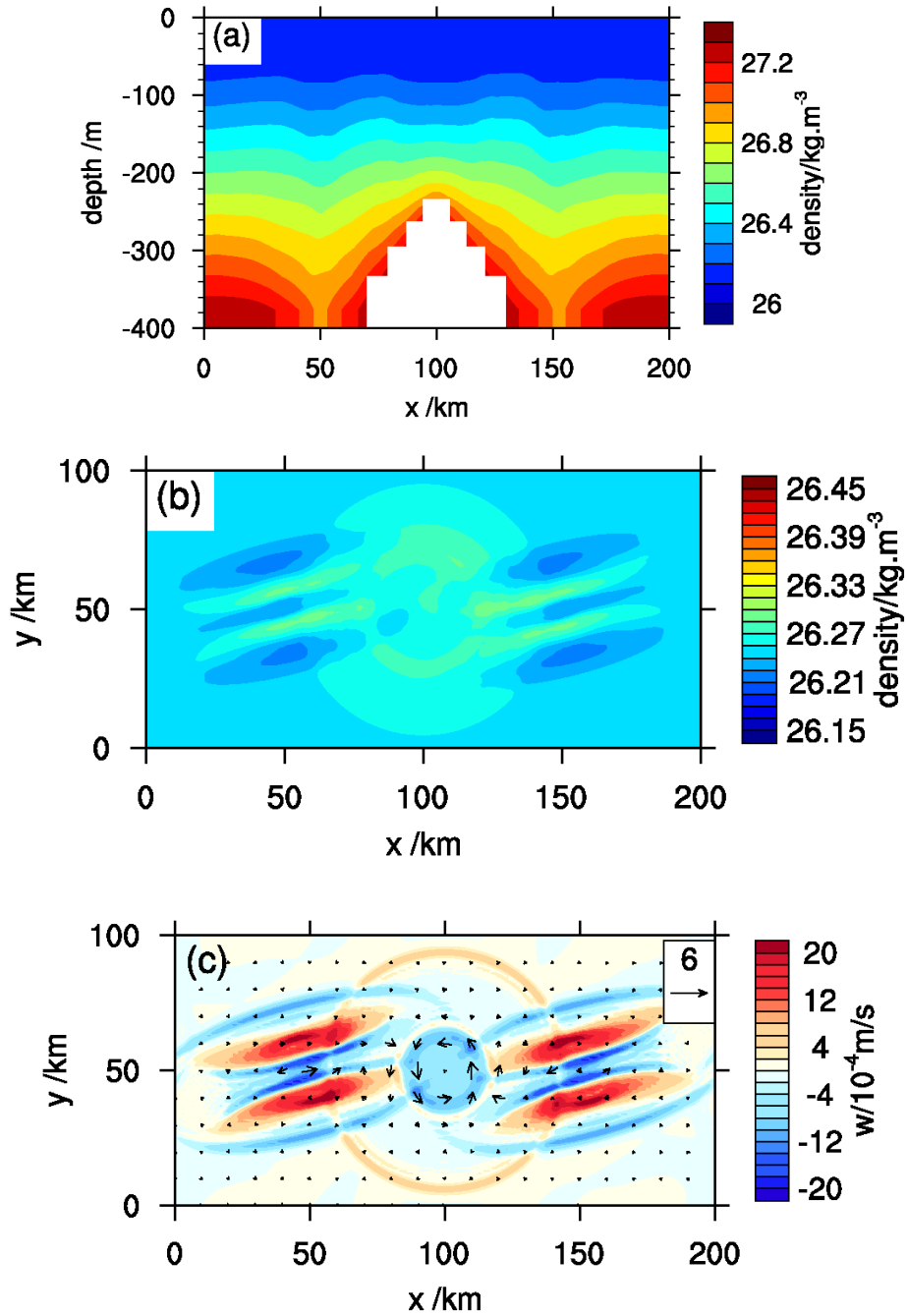832   more evident on September 11, 2013 (not given)

833

Figure Captions

835

836

837

838   Fig.A1. Distribution of the initial density (unit: $kg \cdot m^{-3}$) across the section of y=51

km is shown in (a). Distribution of the initial density (unit: $kg \cdot m^{-3}$) at a depth of 160

m is shown in (b). Distributions of the bottom topography (shaded, unit: m) and the

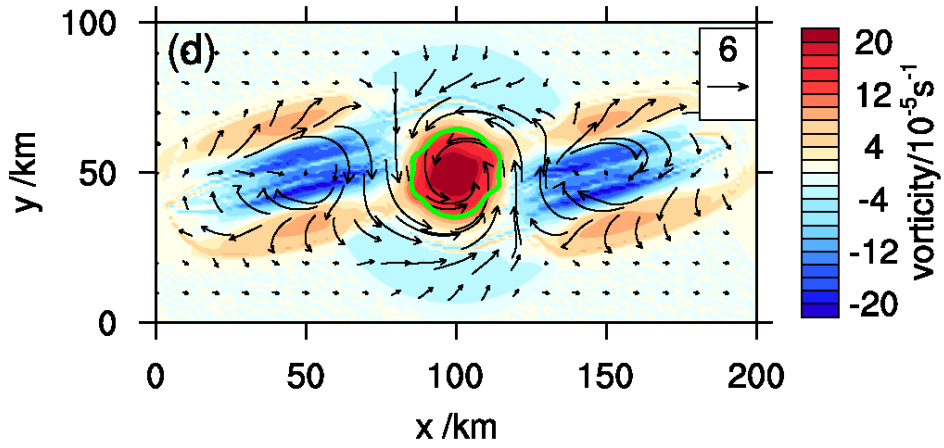wind force (vectors, unit: m/s) are shown in (c).

845

Fig. A2. Distribution of density (unit: $kg \cdot m^{-3}$) across the section of y=51 km at the

6th hour is shown in (a). Distribution of the initial density (unit: $kg \cdot m^{-3}$) at a depth

of 160 m at the 6th hour is shown in (b). Distributions of the vertical averaged velocity

in the horizontal (vectors, unit: cm/s) and vertical (shading, unit: 0.1 mm/s) directions

are shown in (c). Distributions of the surface current (vectors, unit: cm/s) and vertical

vorticity (shading, unit: $10^{-5} \cdot s^{-1}$) are shown in (d).

852

853

854
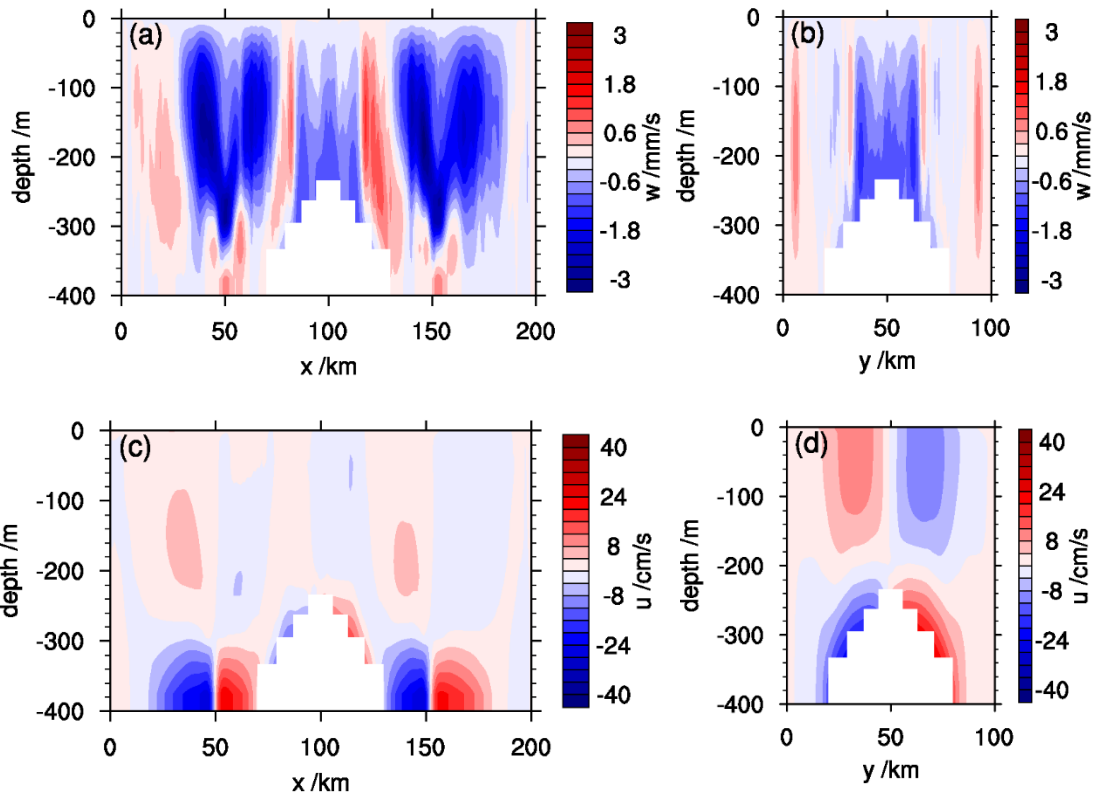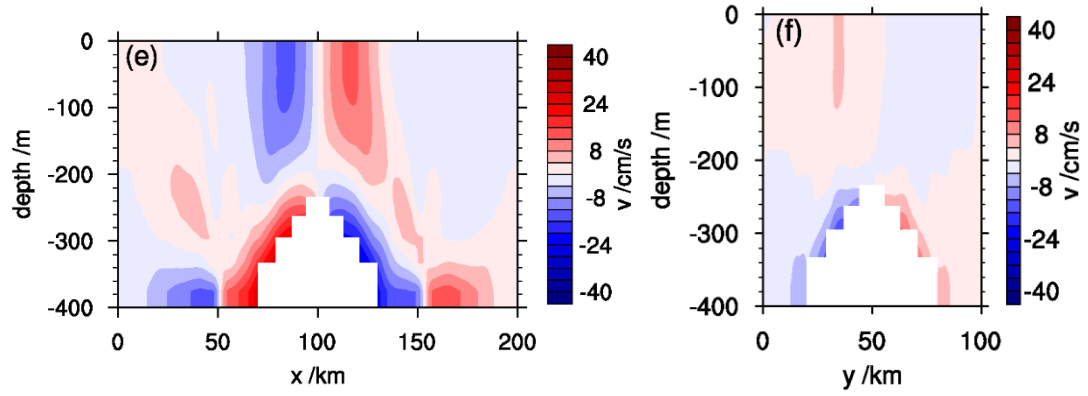
Fig. A3. Distributions of the current velocity across the section of y=50 km in the z, x, and y directions are shown in (a), (c), and (e), respectively. Distributions of the current velocity across the section of x=100 km in the z, x, and y directions are shown in (b), (d), and (f), respectively. Units: u, v cm/s, w, mm/s.
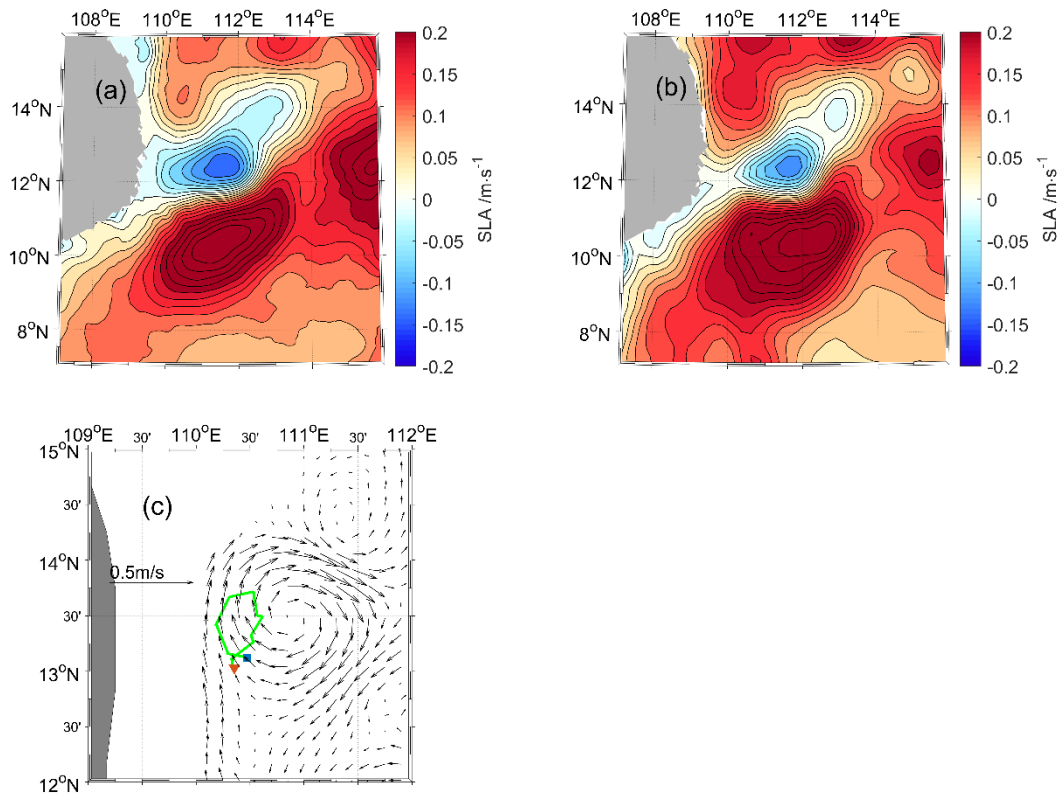

Fig. B1. Distribution of the SLA in our simulation (a) and the AVISO (b) on September 13, 2013, unit: m. The trajectory of Argo No. 5904191 (green line) through the whole September, 2013 and the current field at the layer of -1200 m (vector) on September 13, 2013 are also shown (c).
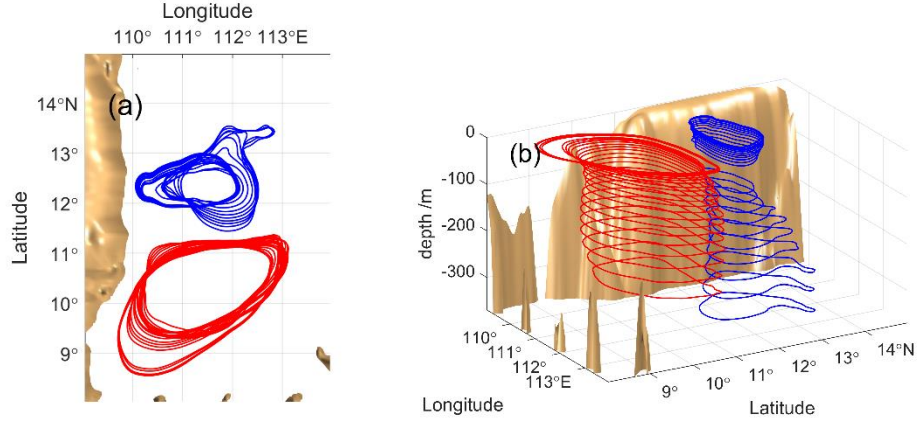
868

869 Fig. B2. Vertical view of the eddy boundary of AE (red line) and CE (blue line) in each

870 layer are shown in (a). 3D structure of the eddy boundary is also shown in (b). The

871 orange shading indicates the topography.
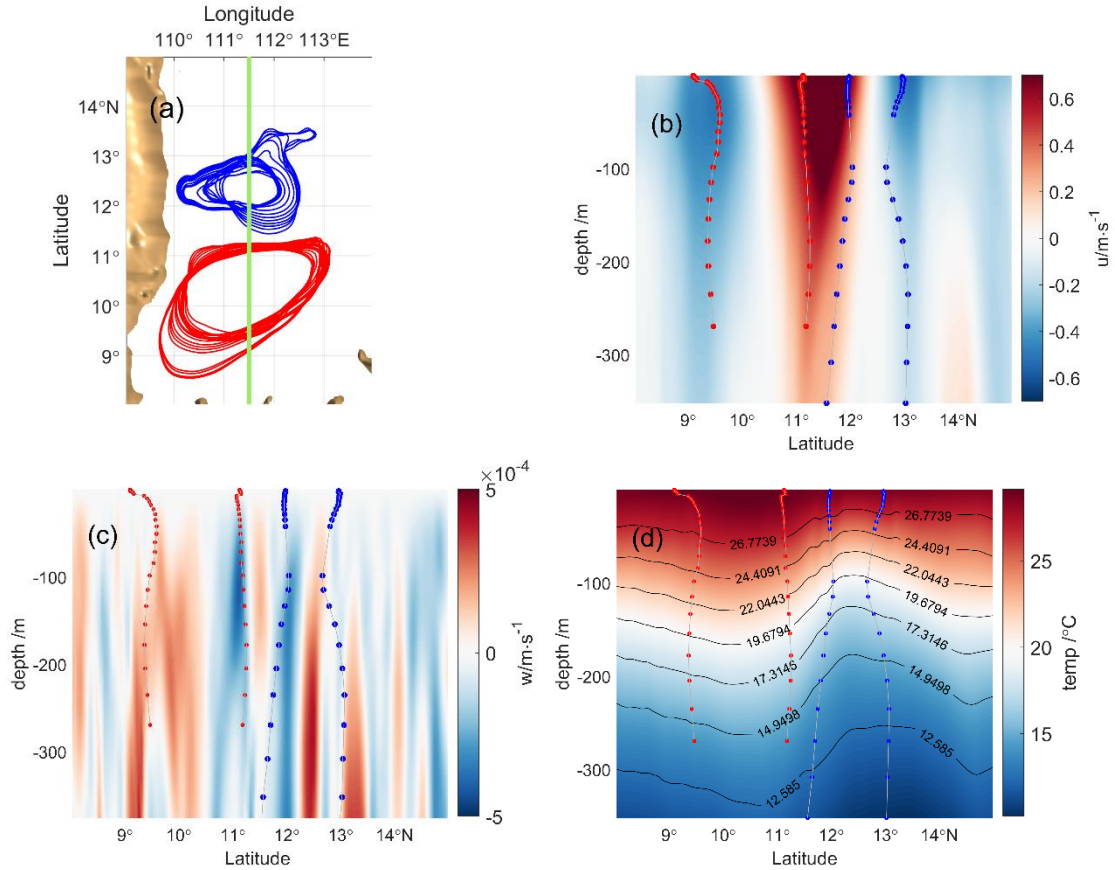

872

873

874 Fig. B3. Vertical view of the eddy boundary of AE (red line) and CE (blue line) in each

875 layer are shown in (a), with a green line nearly across the centers of the two eddies.

876 Along the green line in (a), the vertical profile of the velocity in the zonal (unit: m/s)

877 and vertical direction (unit: 0.1mm/s) are shown as shading in (b) and (c), respectively,

878 while the red and blue dot lines presented the eddy boundary in each layer. The vertical

879 profile of temperature and selected isotherms are shown as shading and contours in (d),
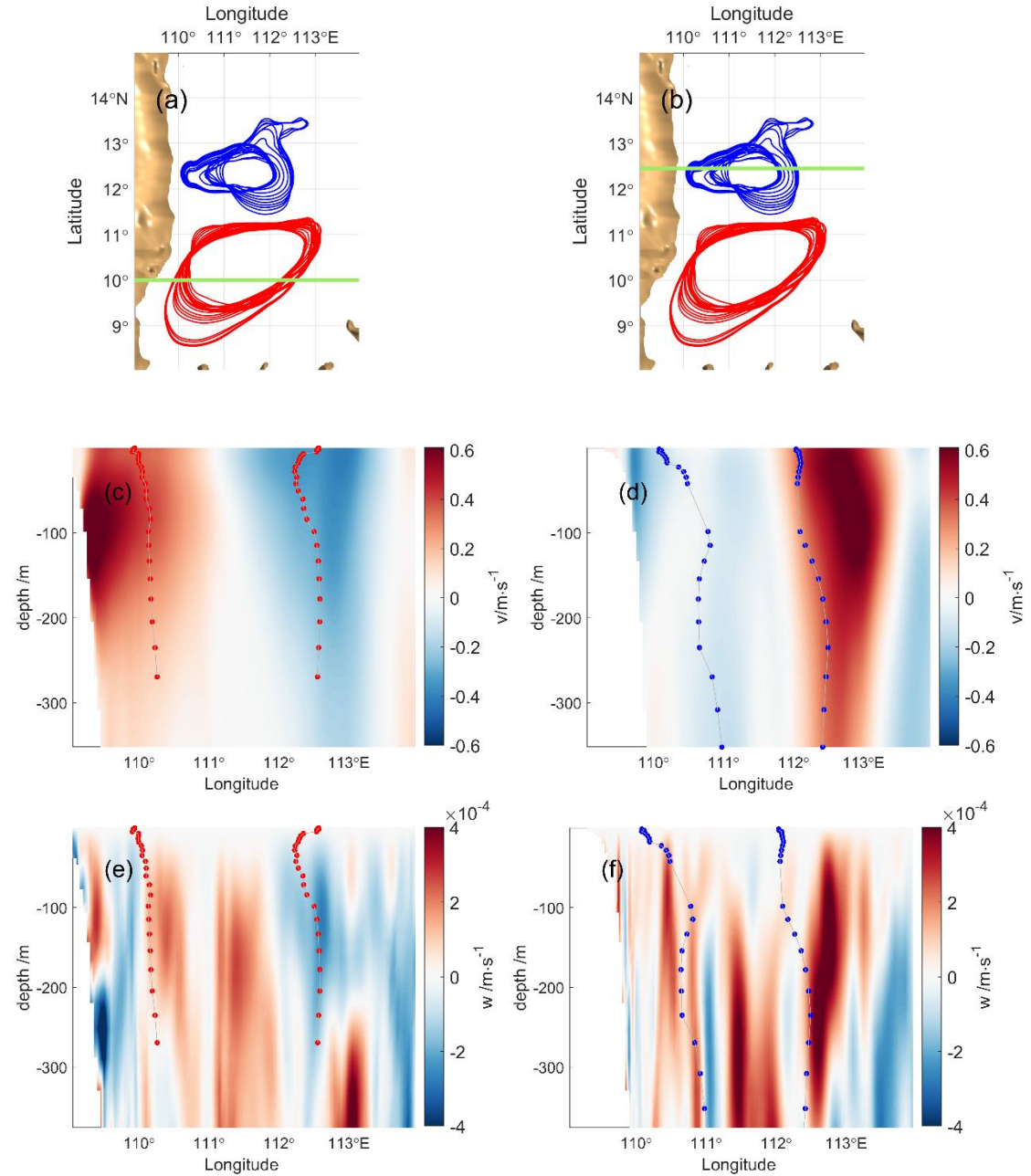
880 unit: °C.

881

882

883

884 Fig. B4. Green line indicates the slice we choose in the AE (a) and CE (b). Along the

885 green line in (a)/(b), the vertical profile of the velocity in the meridional (unit: m/s) and

886 vertical direction (unit: 0.1mm/s) are shown as shading in (c)/(d) and (e)/(f),

887 respectively, while the red and blue dot lines presented the eddy boundary in each layer.

888